known, discussion of the electron and hole properties in the breakdown region must be based on the experimental observations. The behavior of the Hall voltage[5] "saturation" appears to be fit, qualitatively, by a treatment including the influence of the holes produced in breakdown, as mentioned above, over the range 100–1000 V/cm for the applied longitudinal field. In such a treatment, the electron average mobility was assumed to remain unchanged as the current increased. The quality of the fit indicates that this assumption needs only slight modification.

Thus, we have suggested in this paper that in strong electric and magnetic fields, carriers may have sufficient energy in the $\mathbf{E}\times\mathbf{B}$ direction to cause impact ionization—what we call "transverse breakdown," leading to a "saturation" of the Hall voltage. This suggestion has been reinforced by a simple classical phenomenological calculation showing that, for a crystal in which the electron scattering time decreases with energy, electrons of such large energies can occur at applied electric fields lower than in the absence of a magnetic field. Experiments have been performed which show that breakdown is initiated at the point where the Hall voltage saturation occurs and that this Hall field is equal to the required breakdown field for the same magnetic fields but in a geometry which shorts out the Hall field. These results are in agreement with the predictions of the theory.

A better understanding of the impact ionization process requires calculations of the distribution function and experimental tests of its form. Without such a calculation, we cannot treat the magnetoresistance properly, and thus cannot calculate the change in the total breakdown field due to the magnetic field. It is hoped that the considerations presented here will stimulate further more rigorous theoretical treatments of this problem.

ACKNOWLEDGMENTS

We thank Dr. S. Tosima for a number of enlightening discussions and a critical reading of this manuscript, and Dr. R. Hirota for many discussions and suggestions.

PHYSICAL REVIEW VOLUME 140, NUMBER 4A 15 NOVEMBER 1965

Electrical Conductivity in Heavily Doped *n*-Type Germanium: Temperature and Stress Dependence*

MAURICE J. KATZ†‡
IBM Watson Laboratory, Columbia University, New York, New York

(Received 21 May 1965)

Investigations of the piezoresistance of heavily doped *n*-type germanium were made to determine (1) the nature of the carrier scattering mechanisms in degenerate materials and (2) any modification of the conduction-band edge resulting from the large number of impurity states. Stresses large enough to alter the resistivity well beyond the range of linear piezoresistance were applied; saturation of the resistivity at the larger stresses was attained in samples with as many as 10^{19} carriers per cc. Resistivity was measured with extensive parametric variation of dopant, carrier concentration, temperature, and applied stress. The Hall coefficient was also measured as a function of stress for several concentrations. The data are interpreted qualitatively by a four-valley model with a parabolic conduction-band edge, and deviations from this model are discussed. Electron-electron interactions and the temperature dependence of screening contribute significantly to the temperature dependence of the resistivity. The variation of the screening with the relative population of the valley must be considered in interpreting the results of the piezoresistance experiments; in the case of arsenic doping, intervalley scattering is also significant. The mobility anisotropy for screened Coulomb scattering in one valley, as determined from resistivity measurements on antimony-doped samples with large $\langle 111\rangle$ stress, varies with concentration from 5.5 at 1×10^{18} per cc to 3.8 at 1×10^{19} per cc. Evidence for the existence of tail states extending ≈ 0.04 eV below the conduction-band edge is presented.

I. INTRODUCTION

THE discovery of the tunnel diode by Esaki[1] in 1958 has given impetus to both theoretical and experimental investigations of the properties of heavily doped, degenerate semiconductors. Such investigations attempt to answer two questions:

(1) What is the nature of the band structure of semiconductors so heavily doped that the usual simple hydrogenic model for the impurity states no longer holds because of extensive overlap of the ground-state orbitals; and:

(2) What is the nature of the scattering mechanism dominant at such high dopings?

---

* The experimental portion of this investigation was performed at IBM Research Laboratory-Zurich, Ruschlikon ZH, Switzerland.

† William Bayard Cutting Traveling Fellow, Columbia University.

‡ Present address: Los Alamos Scientific Laboratory, University of California, Los Alamos, New Mexico.

[1] L. Esaki, Phys. Rev. **109**, 603 (1958).

Intuitively one expects a large modification of the nature and density of the states in the vicinity of the conduction-band edge. For pure germanium[2] the conduction-band edge consists of four valleys degenerate in energy; light doping with group-V donor impurities causes the formation of localized impurity energy states ≈ 0.01 eV below the conduction band. Heavy doping increases the spatial density of the localized levels; their overlap causes broadening of the impurity levels until they and the original conduction band all merge into one new continuum. It is then that the material is said to be a degenerate[3] semiconductor; the activation energy between impurity states and conduction band no longer exists, and electrons are in the conduction band at all temperatures. In this way the degenerate semiconductor resembles a metal. At low temperatures degenerate Fermi-Dirac statistics will apply, and transport measurements should give detailed information on the energy dependence of the scattering mechanism without the usual Maxwell averaging, i.e., at low temperatures the conductivity of degenerate semiconductors depends on the value of the relaxation time at the Fermi level and not on the functional dependence of the relaxation time on energy as in the usual semiconductor case.

Various theoretical and experimental investigations which elucidate the above questions have been reported. Band-structure calculations for disordered lattices,[4] infrared-absorption experiments,[5,6] measurements of resistivity,[6,7] Hall effect,[5–7] magnetoresistance,[7–9] linear piezoresistance[10] and ultrasonic attenuation[11–13] have all been carried out in heavily doped Ge. High-strain piezoresistance data[3,14–16] which show a saturation of resistivity have also been reported. It is the aim of the present work to report more complete measurements of high-strain piezoresistance and Hall effect together with the temperature dependence of resistivity at various strains and to show their usefulness in explaining the properties of degenerate germanium through simplified models of band structure and scattering mechanisms.

The large value of certain piezoresistance and piezo-Hall-effect tensor components in germanium is due to a change in the relative populations of the four valleys as they shift in energy as a function of applied stress of a particular symmetry.[17] For example, a compressional stress applied in the $\langle 111\rangle$ direction causes three valleys to move to higher energy relative to the fourth, with the result that carriers accumulate in the lowest valley. We expect the resistivity to stop changing when the three raised valleys are above the Fermi level for all the carriers in the lowest valley.

The measurement of large-strain piezoresistance is particularly suited for investigating the properties in which we are interested. The anisotropy of the conductivity may be measured directly in one valley by removing the other three valleys with a large compressive stress in the $\langle 111\rangle$ direction. In the one-valley case the carrier density may be determined directly from the Hall effect without knowledge of the scattering anisotropy as is necessary in the four-valley case.[18] In addition, the behavior of the resistivity and Hall coefficient as they approach their final values should yield information on the density of states near the band edge of the upper three valleys.

An outline of the experimental procedure is given in Sec. II. Results of measurements of resistivity as a function of dopant, carrier concentration, temperature, and stress together with certain piezo-Hall-effect measurements are presented in Sec. III. In Sec. IV, we discuss the analysis and interpretation of the data and attempt to apply various models to explain the experimental results. A summary is presented in Sec. V.

II. EXPERIMENTAL PROCEDURE

Measurements were performed on samples cut from single-crystal germanium pulled from the melt. The samples contained either arsenic or antimony impurities with densities in the range 1×10^{18} to 2×10^{19} per cm^3. Resistivity and Hall effect were measured as a function of temperature on unstrained samples. In addition, three different types of piezoresistance experiments were performed at helium temperatures:

(1) Longitudinal measurements: Resistivity in the $\langle 111\rangle$ direction and Hall voltage perpendicular to the $\langle 111\rangle$ direction were measured as functions of $\langle 111\rangle$ compressional stress using samples of type (1) (see Fig. 1).

(2) Transverse measurements: Resistivity perpendicular to the $\langle 111\rangle$ direction was measured as a function of compressional stress applied in the $\langle 111\rangle$ direction using type (2) samples.

(3) $\langle 1\bar{1}0\rangle$ measurements: Resistivity in the $\langle 1\bar{1}0\rangle$

---

[2] Cf., R. A. Smith, *Semiconductors* (Cambridge University Press, London, 1959), Chap. 10.

[3] Cf., S. H. Koenig, *Proceedings of the International Conference on the Physics of Semiconductors, Exeter 1962* (The Institute of Physics and the Physical Society, London, 1962), p. 5.

[4] Cf., Chapter on Disordered Semiconductors, Ref. 3, p. 205.

[5] C. Haas, Phys. Rev. **125**, 1965 (1962).

[6] W. G. Spitzer, F. A. Trumbore, and R. A. Logan, J. Appl. Phys. **32**, 1822 (1961).

[7] Y. Furukawa, J. Phys. Soc. Japan **16**, 687 (1961).

[8] Y. Furukawa, J. Phys. Soc. Japan **18**, 1374 (1963).

[9] H. Roth, W. D. Straub, W. Bernard, and J. E. Mulhern, Phys. Rev. Letters **11**, 328 (1963).

[10] M. Pollak, Phys. Rev. **111**, 798 (1958).

[11] M. Pomerantz, R. W. Keyes, and P. E. Seiden, Phys. Rev. Letters **9**, 312 (1962).

[12] W. P. Mason and T. B. Bateman, Phys. Rev. Letters **10**, 151 (1963).

[13] W. P. Mason and T. B. Bateman, Phys. Rev. **134**, A1387 (1964).

[14] H. Fritzsche and M. Cuevas, Ref. 3, p. 29.

[15] M. J. Katz, Helv. Phys. Acta **25**, 511 (1962).

[16] M. Cuevas and H. Fritzsche, Phys. Rev. **139**, A1628 (1965).

[17] Cf., S. H. Koenig, *Proceedings of the International School of Physics "Enrico Fermi," Course XXII* (Academic Press Inc., New York, 1963).

[18] C. Herring, Bell System Tech. J. **34**, 237 (1955).

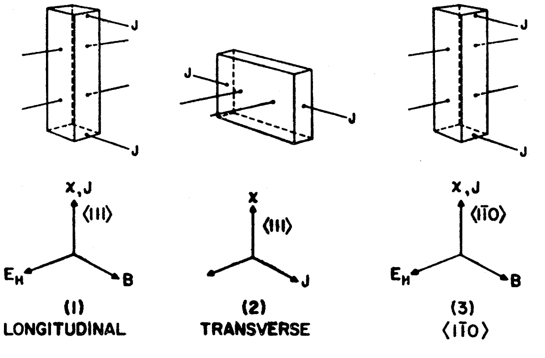

FIG. 1. Sample shape and contact arrangements for the three types of measurements made. Typical sample dimensions are 1.5 mm×1.5 mm×10 mm for types (1) and (3) and 6 mm×1 mm ×4 mm for type (2).

direction was measured as a function of $\langle 1\bar{1}0\rangle$ stress using type (3) samples.

In many of these cases the maximum stress applied was just below the breaking stress, corresponding to a strain of $\approx\frac{1}{2}\%$. In addition, the temperature dependence of resistivity and Hall voltage at several large stresses were measured on some samples.

Brick-shaped samples able to withstand compressional stresses greater than 9000 kg/cm^2 were prepared according to the technique described by Hall.[19] Despite careful preparation it was impossible to construct samples to withstand the stress needed to transfer all carriers to one valley in samples with carrier density greater than about 10^{19} carriers per cm^3. Contacts were made to the sample using pure tin solder dots. Hall effect was measured using a dc current reversing technique.[20] Corrections[21] to the Hall coefficient due to contact geometry were negligible. It was found that most samples had a carrier density inhomogeneity of 5–10% along the length of the sample.

The experiments were performed in an apparatus similar to one described by Hall[19] with one important modification. Because of the large number of measurements to be made, it was necessary to rapidly measure the resistivity as a continuous function of the applied stress. This was accomplished using a constant current supply for the sample current, applying the voltage along the sample to the y axis of an x-y recorder and a voltage proportional to the applied stress to the x axis. The stress voltage was obtained from a commercial load cell in the apparatus between the push rod and the hydraulic system supplying the force. See Fig. 2. A small correction had to be made due to the weight of the push rod. The Hall voltage measurements were made at fixed stresses. A 10-kG magnetic field was produced by a 9-in. Varian magnet powered by a motor-generator power supply. A Kiethley Model 149 Millimicrovoltmeter was used to measure the Hall voltages, and all data were plotted on an Electro-Instrument x-y recorder.

For both resistivity and Hall effect absolute measurements were reliable to 2% while relative resistivity measurements, as a function of stress, were better than 0.5%. Because of poor stability of the power supply the magnetic field was only good to 1%.

Temperature measurements were made with gold-2.1 at.% cobalt to copper thermocouples and with $\frac{1}{10}$-W Allen Bradley resistors calibrated by such thermocouples. The accuracy over the range of temperature measurements was 5%.

III. EXPERIMENTAL RESULTS

A. Resistivity of Unstrained Samples: Dependence on Carrier Concentration

In Fig. 3, the resistivity of unstrained samples ρ_4 at 4.2°K is shown plotted against the carrier density n as determined from the Hall constant at saturation strain. The Hall effect in unstrained germanium depends on the mass and scattering anisotropies of the carriers.[18,22] On the other hand, if we measure the Hall effect in germanium under conditions such that all carriers are in one valley, i.e., under large compressional stress in the $\langle 111\rangle$ direction, the Hall coefficient R_H is readily shown to be independent of mass and scattering anisotropies; $R_H=1/ne$ where e is the charge of the electron in coulombs, and R_H is measured in cm^3 per coulomb.

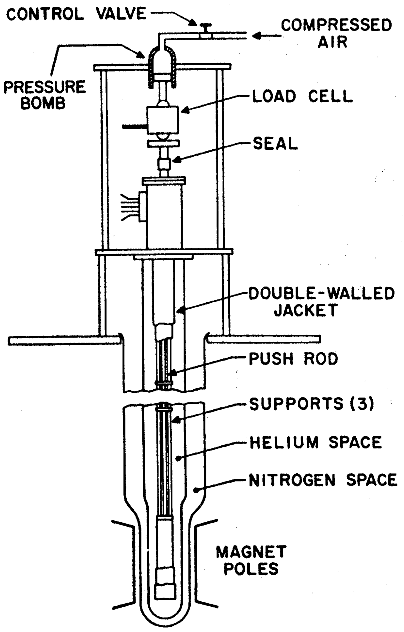

FIG. 2. Apparatus showing method of producing continuously variable stress.

---

[19] J. J. Hall, Phys. Rev. **128**, 68 (1962).

[20] S. J. Angello, Phys. Rev. **62**, 371 (1942).

[21] I. Isenberg, B. R. Russell, and R. F. Greene, Rev. Sci. Instr. **19**, 685 (1948).

[22] C. Herring and E. Vogt, Phys. Rev. **101**, 944 (1956).

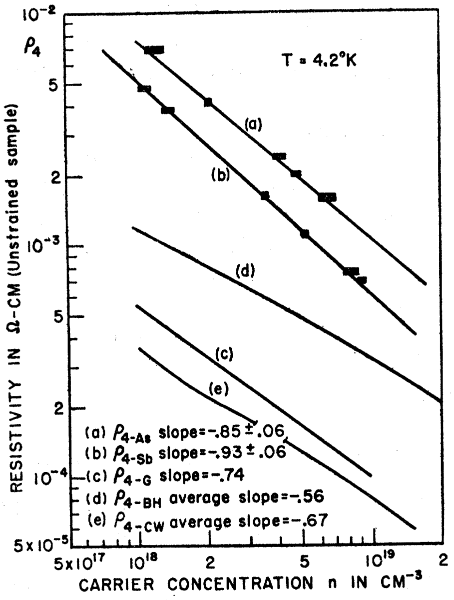

FIG. 3. Experimental data for resistivity of unstrained material, (a) and (b), versus carrier concentration together with curves calculated from models discussed in Appendix A. Experimental errors are indicated by the sizes of the points.

Implicit in using this n is the assumption that the total carrier density is independent of stress.

The experimental data in Fig. 3 show that the ρ_4-versus-n behavior for both arsenic- and antimony-doped samples are similar in the region of $n=10^{18}$-10^{19} cm^{-3}, with $\rho\propto n^{-0.9}$ but differ by a factor of about 1.6 over that range, the resistivity of the samples doped with arsenic being greater than those with antimony. The resistivity ratio $\rho_{4\text{–As}}/\rho_{4\text{–Sb}}$ increases slightly with increasing n.

The resistivity and the mobility μ are related as $\rho=(ne\mu)^{-1}$ and in an independent-scatter model

$$\mu^{-1}\propto na(v_F)\,, \qquad (1)$$

where v_F is the Fermi velocity and the concentration of scattering centers is assumed equal to the carrier concentration. For a temperature of 0°K the Fermi velocity is proportional to $n^{+1/3}$ and the isotropic Rutherford scattering model[23] predicts $a(v_F)\propto v_F^{-3}$. From the Fig. 3 data, we find for antimony doping $a(v_F)\propto v_F^{-(2.8\pm0.2)}$ and for arsenic doping $a(v_F)\propto v_F^{-(2.6\pm0.2)}$. (The exponent in the arsenic case differs somewhat from that found by Koenig[3] because in the present work n is determined from the saturation-stress Hall coefficient.)

B. Resistivity of Saturated Samples: Dependence on Carrier Concentrations

As stated above, large compressive stress in the ⟨111⟩ direction raises three of the valleys in energy, transferring all the carriers into the lowest valley. When the Hall voltage, measured as a function of the applied stress, stops changing we assume that all the carriers have been transferred to the lowest valley. The sample is then said to be saturated. The resistivity also approaches a constant value at high stresses. For antimony-doped material the final resistivity is reached at the saturation stress, but in arsenic-doped material higher stresses are needed. ρ_3, the final resistivity parallel to the ⟨111⟩ direction (the axis of rotation of the lowest valley), may be measured using longitudinal samples. The final resistivity perpendicular to this axis ρ_1 may be measured using transverse samples. Results of such measurements made at liquid-helium temperature are shown in Figs. 4 and 5.

The helium-temperature data for ρ_3 and ρ_1 are similar to those of ρ_4. In all cases, ρ varies approximately inversely as n, with the resistivity of the arsenic-doped material from 1 to 2 times as great as the antimony-doped material, this ratio increasing for increasing n. Following Eq. (1), we find in the ρ_1 case, $a(v_F)\propto v_F^{-(3.0\pm0.1)}$ for antimony doping and $a(v_F)\propto v_F^{-(2.7\pm0.3)}$ for arsenic doping. In the ρ_3 case $a(v_F)\propto v_F^{-3.6}$ for antimony doping and $a(v_F)\propto v_F^{-3.0}$ for arsenic doping.

C. Resistivity of Unstrained Samples: Temperature Dependence

The resistivity of unstrained material was measured as a function of temperature in the range 4.2–250°K for five antimony-doped samples and seven doped with arsenic. Typical results are shown in Figs. 6 and 7.

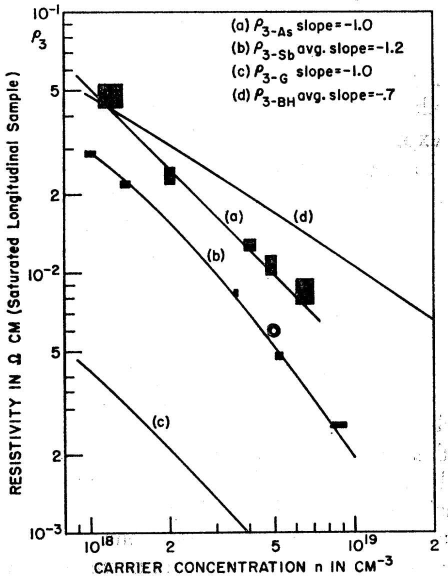

FIG. 4. Experimental data for the final resistivity of stressed longitudinal samples, (a) and (b), versus carrier concentration together with curves calculated from models discussed in Appendix A. Lack of machine storage precluded calculation of $\rho_{4\text{–CW}}$ to the desired accuracy.

---

[23] Cf., N. F. Mott and H. S. W. Massey, *The Theory of Atomic Collisions* (Oxford University Press, London, 1949), 2nd ed., Chap. III.

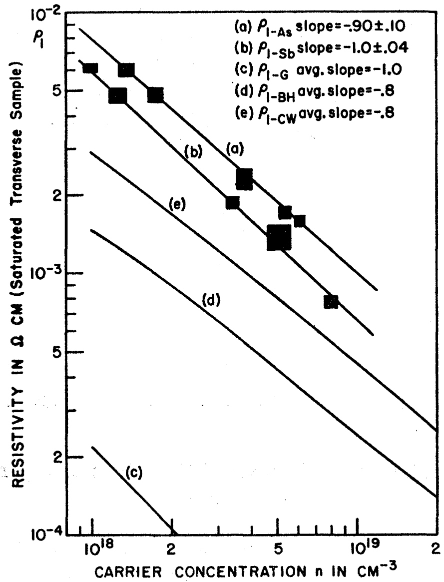

FIG. 5. Experimental data for the final resistivity of stressed transverse samples, (a) and (b), versus carrier concentration together with curves calculated from models discussed in Appendix A.

For all samples, the resistivity initially increased with temperature even at the lowest temperatures. The samples with the least impurities showed a hump in the $\rho_4(T)$ curve at about 70°K which is below the degeneracy temperature, i.e., the temperature equivalent of the Fermi level for an ambient temperature of 0°K. More highly doped samples showed resistivity increasing even at temperatures higher than the degeneracy temperature.

It is informative to present the $\rho_4(T)$ data by plotting $\Delta\rho_4/\Delta\rho_4(0)\equiv[\rho_4(T)-\rho_4(0)]/\rho_4(0)$ versus T/T_D, where T_D is the degeneracy temperature. At low temperatures T_D corresponds to the energy of the carriers involved in transport. The data thus reduced are shown in Figs. 8 and 9. It is seen that the $\Delta\rho_4/\rho_4(0)$ versus T/T_D behavior is fairly consistent over the range plotted for all concentrations of a given dopant, the increase in resistivity being slightly higher for the Sb-doped material.

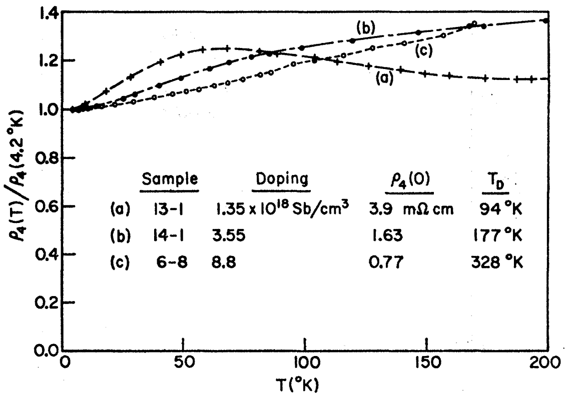

FIG. 6. Resistivity versus temperature for unstrained antimony-doped samples. $\rho_4(0)$ is the extrapolated value at 0°K. T_D is the degeneracy temperature.

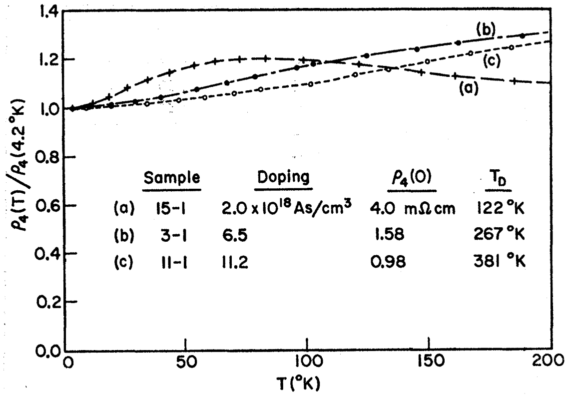

FIG. 7. Resistivity versus temperature for unstrained arsenic-doped samples.

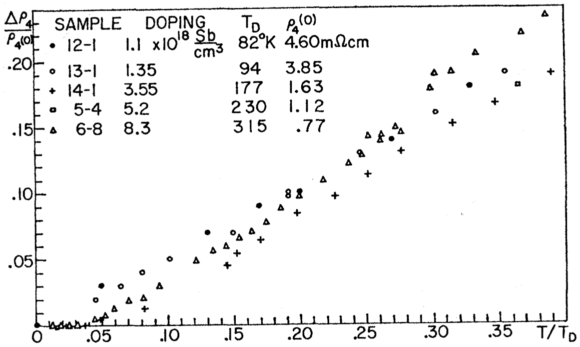

FIG. 8. Increment in resistivity for unstrained antimony-doped samples versus temperature normalized to T_D.

Morgan[24] has recently observed that the temperature dependence of resistivity in degenerate semiconductors is proportional to the Bose-Einstein distribution func-

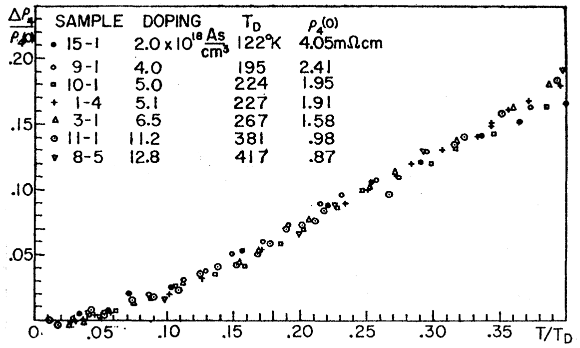

FIG. 9. Increment in resistivity for unstrained arsenic-doped samples versus temperature normalized to T_D.

---

[24] T. N. Morgan (unpublished).

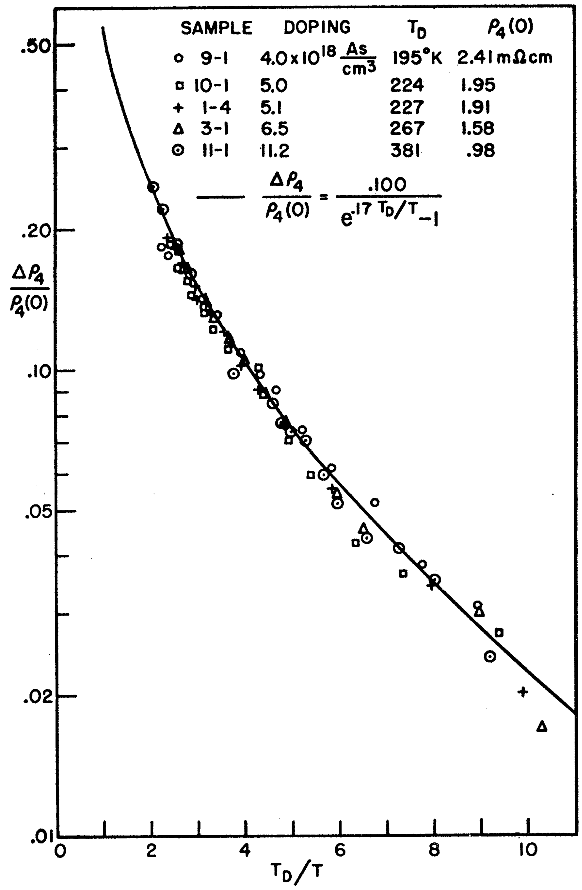

FIG. 10. Bose-Einstein function fit to the experimental values of incremental resistivity versus T_D/T.

tion. In the region $0.1<T/T_D<0.5$ our data for arsenic doping satisfy the relation

$$\frac{\rho_4(T)-\rho_4(0)}{\rho_4(0)}=\frac{0.100}{e^{0.17T_D/T}-1}$$

independent of T_D, as shown in Fig. 10.

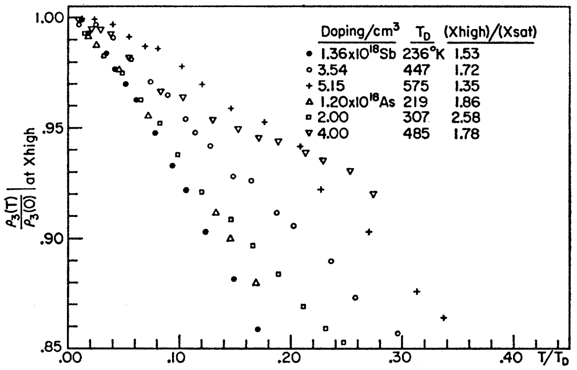

FIG. 11. Longitudinal resistivity at high stress versus T/T_D.

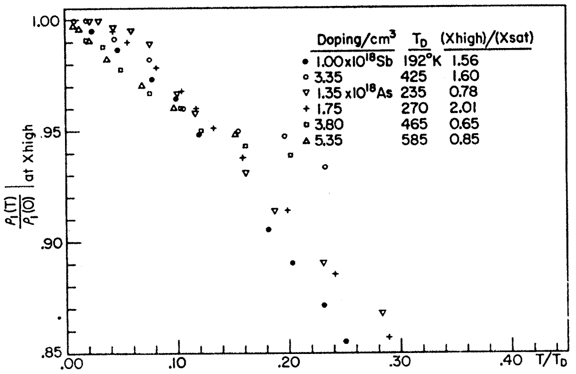

FIG. 12. Transverse resistivity at high stress versus T/T_D.

D. Resistivity of Saturated Samples: Temperature Dependence

The temperature dependence of ρ_3 and ρ_1 was measured at various stresses including those at and above the stress needed for depopulation of the higher three valleys at $T=0$. The data for various samples at the greatest stresses for which measurements were made are plotted as $\rho/\rho(0°\text{K})$ versus T/T_D in Figs. 11 and 12. It is seen that in all cases the resistivity decreases with increasing temperature and for a given dopant at a given T/T_D the relative resistivity increases for increasing carrier concentration.

Resistivity as a function of temperature at various post-saturation stresses on a given sample was also measured. In the ρ_3 case, the measurements showed the $\rho_3(T)/\rho_3(0)$ behavior to be initially the same at all post saturation stresses. As temperature increases a temperature is reached where the $\rho_3(T)/\rho_3(0)$ curve for a given stress begins to decrease more rapidly than the common curve for all higher stresses. An example of this behavior is shown in Fig. 13. It was also possible to apply two unequal but very high stresses to a given

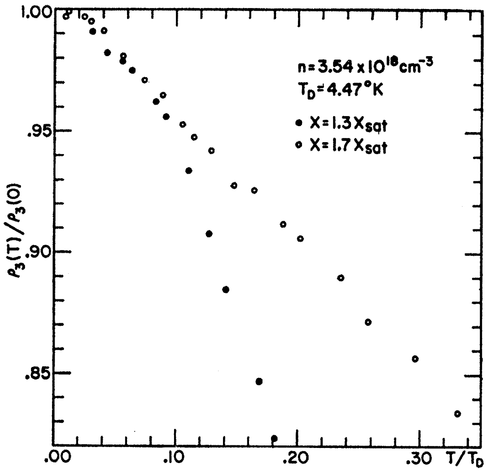

FIG. 13. Longitudinal resistivity versus T/T_D at high stresses.

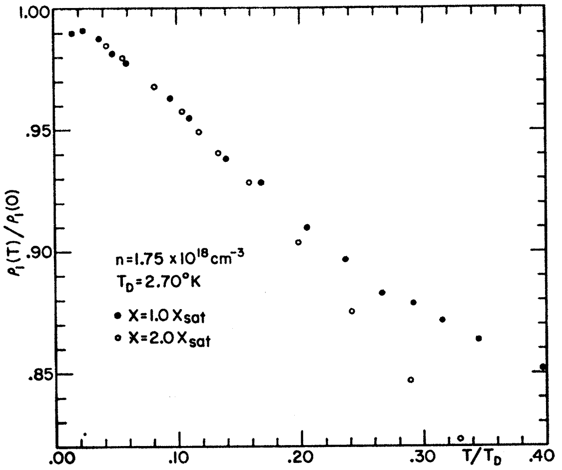

FIG. 14. Transverse resistivity versus T/T_D at high stresses.

sample such that the $\rho_3(T)/\rho_3(0)$ behavior was the same for both throughout the range of measurement.

The $\rho_1(T)/\rho_1(0)$ data showed similar behavior except that departures from the common high stress curve of the lower strain data was in the direction of increasing resistivity. See Fig. 14.

E. Piezoresistance Experiments in Antimony-Doped Material

(a) *Longitudinal Measurements*

Using samples of the longitudinal type, the resistivity ρ_L and Hall coefficient R_H were measured at 4.2°K as functions of stress for 5 samples with dopant concentrations between 1.1 and 9.1×10^{18} per cm^3. Saturation was achieved in all cases. Stress as high as 9000 kg/cm^2 ($\approx9\times10^9$ dynes/cm^2) corresponding to a strain of about 0.5% was successfully applied without sample fracture. The Hall voltage measured near both ends of the sample indicated inhomogeneities in carrier concentration between 1 and 10%. As expected, in all samples, the stress needed to saturate the Hall coefficient was higher at the end with higher impurity concentration.

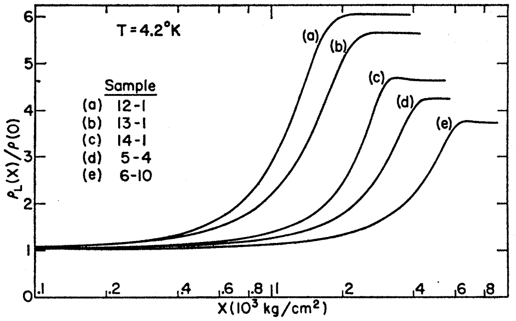

FIG. 15. Longitudinal resistivity versus stress for antimony-doped samples. Curves shown are reduced copies of the data as plotted on an X-Y recorder.

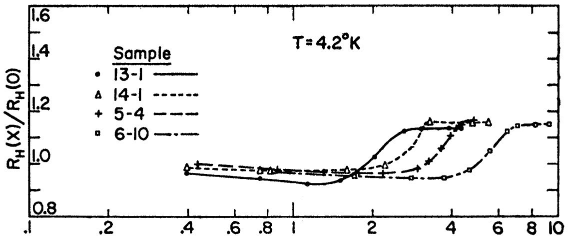

FIG. 16. Hall coefficient versus stress for antimony-doped samples. The experimental points are connected for clarity.

The resistivity as a function of stress is plotted in Fig. 15; the Hall coefficient in Fig. 16. The resistivity and both Hall coefficients as measured for a particular sample are plotted in Fig. 17. All samples similarly reached their final resistivities at stresses close to the saturation stress for the more highly doped end. All measurements are normalized to their zero-stress values.

By sliding the logarithmic resistivity plots over one another along the stress axis, it may be shown that the curves all have the same shape, except for their behavior near saturation; the ratio of final to initial resistivities being smaller for higher dopings. The Hall-coefficient data, on the other hand, show the same behavior throughout, initially decreasing, passing through a minimum, increasing, and finally all of them saturating at a value of 1.15 times the initial one.

The results of the longitudinal measurements are summarized in Table I.

(b) *Transverse Measurements*

The resistivity ρ_T was measured as a function of stress at 4.2°K using samples of the transverse type. Data were obtained for four samples in the range 1-8×10^{18} carriers per cm^3 and plotted in Fig. 18. Hall effect was not measured; the doping was determined from the zero-stress resistivity.

The curves show similar behavior in all cases, decreasing initially, passing through a minimum and

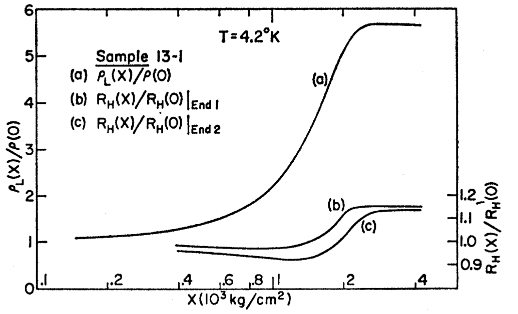

FIG. 17. Resistivity and Hall coefficients measured near both ends of a longitudinal antimony doped sample versus stress. The resistivity curve is traced from a recorder plot. The Hall-effect curves are smooth curves drawn through the data points (not shown).

TABLE I. Summary of data for longitudinal piezoresistance measurements on antimony-doped samples. Two values in one column refer to measurements near different ends of the sample.

Sample	$\rho(0)$ (mΩ cm)	n (10^{18} cm^{-3})	$X_{\text{final}}\left(10^3 \frac{\text{kg}}{\text{cm}^2}\right)$	$\rho_{\text{final}}/\rho(0)$	$X_{\text{sat}}\left(10^3 \frac{\text{kg}}{\text{cm}^2}\right)$	$R_H(\text{sat})/R_H(0)$
12–1	4.74	1.04–1.15	2.2	6.04		1.15 1.15
13–1	3.85	1.31–1.41	2.6	5.65	2.35 2.7	1.14 1.15
14–1	1.63	3.53–3.55	3.3	4.70	3.3 3.3	1.15 1.16
5–4	1.12	5.07–5.22	4.5	4.25	4.3 4.6	1.15 1.16
6–10	0.695	8.95–9.33	6.6	3.75	6.3 6.8	1.15

increasing until the final resistivity. The saturation is not as sharp as in the ρ_L case and samples 14–2 and 6–11 reach their final resistivities at stresses higher than those expected from the ρ_L data. This is most probably due to clamping of the sample ends which created a stress perpendicular to the $\langle 111\rangle$ direction which, due to the shortness of the sample, creates additional strains in the region of measurement such that higher $\langle 111\rangle$ stress is needed for complete valley depopulation. In addition, the contact geometry for resistivity measurements is poor in this case and a systematic error that gives higher resistivity values, thereby implying lower doping and saturation stress, may have been introduced. In any event, the final resistivity ratios are reliable. Transverse data are summarized in Table II.

(*c*) *Measurements on $\langle 1\bar{1}0\rangle$ Samples*

Resistivity of $\langle 1\bar{1}0\rangle$ samples was measured as a function of stress at 4.2°K in five samples with carrier concentration in the range 1-9$\times 10^{18}$ carriers per cm^3. The Hall coefficient for these samples was measured at zero stress only and the concentration determined from similar data in the longitudinal case. Data are plotted in Fig. 19 and summarized in Table III. As in the longitudinal case, all curves have the same behavior except near saturation where the final resistivity ratio decreases as the carrier concentration increases.

F. Piezoresistance Measurements in Arsenic-Doped Material

(*a*) *Longitudinal Measurements*

Measurements of the type described in Sec. III. E(*a*) were made in arsenic-doped material. Satisfactory data for ρ_L were obtained for 7 samples in the range 1–15 $\times 10^{18}$ carriers per cm^3, however, saturation was not attained in all samples. The major difference between the ρ_L curves in the arsenic and antimony data is that for all antimony samples $\rho_L(X)$ shows a peak at a stress about 20% below the saturation stress. The final resistivity, which would be achieved at a stress well above X_{sat}, was not attained in the antimony case and both ρ_{final} and X_{final} had to be extrapolated from the lower stress data.

TABLE II. Summary of data for transverse-piezoresistance measurements on antimony-doped samples.

Sample	$\rho(0)$ (mΩ cm)	n (10^{18} cm^{-3})	X_{final} (10^3 kg/cm^2)	$\rho_{\text{final}}/\rho(0)$
12–2	$\approx$5.34	$\approx$1.00	2.1	1.143
13–2	$\approx$4.23	$\approx$1.25	2.5	1.127
14–2	$\approx$1.70	$\approx$3.40	3.7	1.098
6–11	$\approx$0.76	$\approx$8.00	7.5	1.014

With the exception of one sample, the ratio of peak resistivity to zero resistivity decreases with increasing doping. The final resistivity ratio also appears to be decreasing. The value of the stress at the peaks, X_{peak}, increases with increasing doping. What seems most strange is that the final resistivity is reached long after saturation, as determined by the Hall coefficient, is attained. In addition, the final Hall-coefficient ratio increases from a value of 1.04 for $n=1.1\times 10^{18}$ per cm^3 to 1.11 at 7×10^{18}.

Data for these measurements are shown in Figs. 20, 21, and 22 and summarized in Table IV.

(*b*) *Transverse Measurements*

Measurements of ρ_T as a function of stress were made at 4.2°K for seven samples in the range 1.4-15 $\times 10^{18}$ carriers per cm^3. As in the longitudinal case, peaks were found in the resistivity versus stress data. The behavior of all the curves was similar, initially decreasing, passing through a minimum, increasing to a peak, and decreasing toward a final resistivity. The final resistivity, however, was not attained in any of the measurements. As in the longitudinal case X_{peak} increases and with one exception the ratio $\rho_{\text{peak}}/\rho(0)$ decreases with increasing doping. Aside from peaking the main difference between the behavior of ρ_T in the antimony and arsenic cases is that the final resistivity ratio for a given dopant concentration is significantly lower in the arsenic case.

TABLE III. Summary of data for $\langle 1\bar{1}0\rangle$ piezoresistance measurements on antimony-doped samples. Two values in one column refer to measurements near different ends of the sample.

Sample	$\rho(0)$ (mΩ cm)	n (10^{18} cm^{-3})	X_{final} (10^3 kg/cm^2)	$\rho_{\text{final}}/\rho(0)$
12–4	4.97	0.99–1.02	1.4	2.12
13–3	4.34	1.19–1.20	1.85	2.10
14–3	1.79	3.08–3.23	3.0	2.05
5–5	1.15	5.20–5.23	4.0	1.99
6–12	0.81	8.11–8.14	5.1	1.94

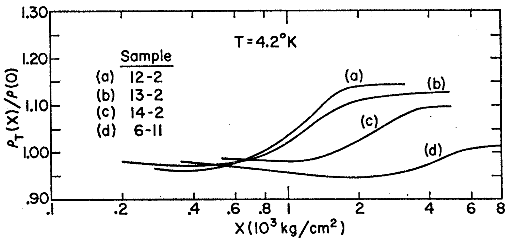

FIG. 18. Transverse resistivity versus stress for antimony-doped samples. Curves shown are traced from X-Y recorder plots.

Data for these measurements are shown in Fig. 23 and summarized in Table V.

(c) $\langle 1\bar{1}0\rangle$ *Measurements*

These measurements were made on 6 samples with carrier concentration in the range $1\text{-}14\times10^{18}$ per cm^3. As the other arsenic data, these too showed a peak. All curves showed similar behavior and by shifting the logrithmic axes could be brought into conjugance, except in the region of the peaking. $X_{\rm peak}$ increases with increasing doping and $\rho_{\rm peak}/\rho(0)$ decreases. Data at very high strains were not taken in this case and, therefore, $\rho_{\rm final}$ and $X_{\rm final}$ were not determined. Data for these measurements are shown in Fig. 24 and summarized in Table VI.

G. Linear Piezoresistance

Although the apparatus was not designed for this purpose, it was possible to obtain values for the linear piezoresistance in some of the longitudinal and $\langle 1\bar{1}0\rangle$ samples by measuring the initial slope of the $\rho(X)/\rho(0)$ data. This was not possible in the transverse case. Values for $[\rho(X)-\rho(0)]/\rho(0)X$ are given in Table VII (X is negative for compressional stress), and are good to better than 10%.

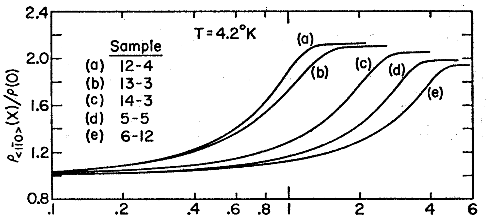

FIG. 19. $\langle 1\bar{1}0\rangle$ resistivity versus stress for antimony-doped samples. Curves shown are traced from X-Y recorder plots.

H. Magnetoresistance

Even though the sensitivity of the apparatus was not good enough to yield quantitative results, an attempt was made to measure and compare the transverse magnetoresistance in unstrained and saturated longitudinal samples. The magnetoresistance in unstrained material was to small to be measured with our equipment. However, a definite negative magnetoresistance was observed in the one-valley case. The data are given in Table VIII.

IV. DISCUSSION

A. Resistivity of Unstrained Material: Dependence on Carrier Concentration at 4.2°K

At the present time, there is no quantitative explanation of the ρ-versus-n data. No one model is available that fits all the aspects of the physical situation. Scattering models that have been extensively discussed usually assume that the scattering centers scatter independently. Since from Fig. 25, the de Broglie wavelength of the carriers in the range of interest is greater than the average interimpurity distance, any postulated completely independent scatterer model is unjustified. Collision theory usually discusses two extreme cases, those for which the product of the carrier's wave number and the effective distance at which the potential is cut off is either very much greater than or very much less than unity. Figure 26 shows that for our case neither condition is satisfied. It is nevertheless instructive to examine the ρ-versus-n behavior for the various models considered in the literature.

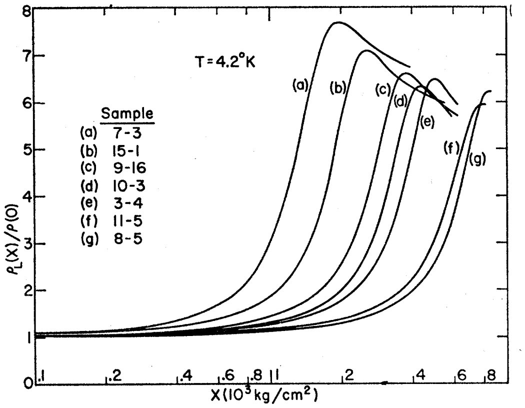

FIG. 20. Longitudinal resistivity versus stress for arsenic-doped samples. Curves shown are traced from X-Y recorder plots.

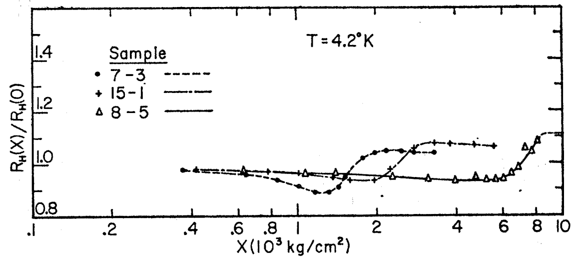

FIG. 21. Hall coefficient versus stress for arsenic-doped samples. Experimental points are connected for clarity.

TABLE IV. Summary of data for longitudinal-piezoresistance measurements on arsenic-doped samples. Two values in one column refer to measurements near different ends of the sample.

Sample	$\rho(0)$ (mΩ cm)	n (10^{18} cm^{-3})	X_{peak} (10^3 kg/cm^3)	$\rho_{\text{peak}}/\rho(0)$	X_{final} (10^3 kg/cm^2)	$\rho_{\text{final}}/\rho(0)$	X_{sat} (10^3 kg/cm^2)	$R_H(\text{sat})/R_H(0)$
7–3	6.96	1.10–1.30	2.00	7.67	6–7	6.0–6.5	2.1 2.4	1.04 1.05
15–1	4.07	1.95–2.06	2.57	7.08	6.5–6.6	5.8–6.0	2.8 3.2	1.05 1.07
9–1*b*	2.38	3.81–4.20	3.79	6.61	7.5–9	5.4–5.7	$\approx$4.5 4.5	1.07 1.08
10–3	2.02	4.72–4.96	4.34	6.32	$>$7	$<$5.5		1.08
3–4	1.58	5.99–6.95	5.00	6.51	$>$8	$\approx$5.5	6.2 $>$6	1.11
11–5	1.00	$\approx$11–$\approx$14	8.20	5.94	$>$8			
8–5	0.87	$\approx$15	8.54	6.24	$>$9		$>$8 $>$8	$\approx$1.1

The data shown in Fig. 3 were taken at $T=4.2$°K. Assuming parabolic conduction bands with the density-of-states mass appropriate to the pure material, the degeneracy temperature for four-valley germanium is in the range 80 to 350°K for doping concentration between 10^{18} and 10^{19} carrier per cm^3, see Fig. 27. Therefore, it is appropriate to assume complete Fermi degeneracy of the carriers in the conduction band. In addition, the low ambient temperature excludes the possibility of a significant contribution of lattice scattering, the lattice mobility being orders of magnitude greater than those we measure.[25] The main scattering mechanism we need be concerned with is that of ionized impurity scattering—the concentration of ionized impurities being the same as that of the carriers, since none of the doping was compensated during growth.

Two extreme cases of ionized impurity scattering have been discussed in the literature. They depend on the ratio of the de Broglie wavelength of the carriers to the range of the scattering potential. Let k be the carrier wave number and a be the range of the scattering potential. The case for $ka\gg 1$ has been discussed classically by Conwell and Weisskopf,[26] who used the Rutherford scattering-formula cut off for small-angle scattering, and independently by Brooks, and Herring,[27] and Dingle,[28] who use the Born approximation and a screened Coulomb field. The case for $ka\ll 1$ was treated by Csavinszky[29] and by Gulyaev.[30] Both authors used a screened Coulomb potential to determine the s-wave phase shift by variational techniques. Higher order phase shifts were neglected.

All the above authors assumed isotropy of the band structure, spherical energy surfaces, and an isotropic scattering potential in their calculations; the anisotropy and many-valleyed nature of the conduction band were neglected. We have repeated the calculations and included the effective mass tensor and four-valley geometry appropriate to germanium. To do this, one first considers an incoming wave along a principle axis of the mass tensor and transforms to a "spherical" space with the density-of-states mass. The scattering potential, though spherical in the original coordinates is ellipsoidal in the "spherical" space. This does not effect the calculation in the Born approximation except to complicate the integrations. On the other hand, the method of partial waves depends on a spherical scattering potential. However, for $ka\ll 1$ the de Broglie wavelength is much larger than the range of the

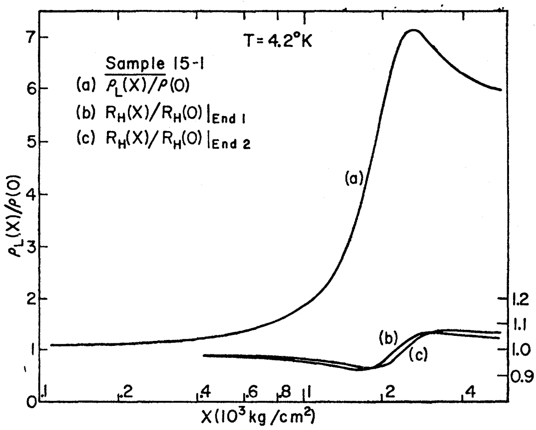

FIG. 22. Resistivity and Hall coefficients measured near both ends of a longitudinal arsenic-doped sample versus stress. The resistivity curve is traced from a recorder plot. The Hall-effect curves are smooth curves drawn through the data points (not shown).

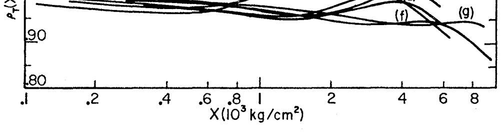

FIG. 23. Transverse resistivity versus stress for arsenic-doped samples. Curves shown are traced from X-Y recorder plots.

---

[25] Cf., S. H. Koenig, R. D. Brown, III, and W. Schillinger, Phys. Rev. **128**, 1668 (1962).

[26] E. Conwell and V. F. Weisskopf, Phys. Rev. **69**, 258 (1946); **77**, 388 (1950).

[27] Cf., P. P. Debye and E. M. Conwell, Phys. Rev. **93**, 693 (1954).

[28] Cf., R. B. Dingle, Phil. Mag. **46**, 831 (1955).

[29] P. Csavinsky, Phys. Rev. **126**, 1436 (1962); **131**, 2033 (1963); **135**, AB3 (1964).

[30] Yu V. Gulyaev, Fiz. Tverd. Tela **1**, 422 (1959) [English transl.: Soviet Phys.—Solid State **1**, 381 (1959)].

TABLE V. Summary of data for transverse-piezoresistance measurements on arsenic-doped samples.

Sample	$\rho(0)$ (mΩ cm)	n (10^{18} cm^{-3})	X_{peak} (10^3 kg/cm^2)	$\rho_{\text{peak}}/\rho(0)$	X_{final} (10^3 kg/cm^2)	$\rho_{\text{final}}/\rho(0)$
7–2	≈5.94	≈1.4	1.82	1.12	5–7	0.98–1.10
15–3	≈4.78	≈1.7	2.13	1.08	5.5–6.5	0.99–1.00
9–2	≈2.48	≈3.8	3.18	1.00	>6	<0.95
10–4	≈1.85	≈5.3	3.81	0.99	>6.5	<0.93
3–3	≈1.66	≈6.1	4.03	1.02	>6.5	<0.97
11–6	≈1.16	≈9.2	5.33	0.95	>9.5	<0.85
8–4	≈0.81	≈14.	7.44	0.95	>9.0	<0.93

potential, the scattering will be mainly s wave and not be affected by the structural anisotropy of the scattering potential. This has been shown rigorously by Gutzwiller.[31]

TABLE VI. Summary of data for $\langle 1\bar{1}0\rangle$ piezoresistance measurements on arsenic-doped samples. Two values in one column refer to measurements near different ends of the sample.

Sample	$\rho(0)$ (mΩ cm)	n (10^{18} cm^{-3})	X_{peak} (10^3 kg/cm^2)	$\rho_{\text{peak}}/\rho(0)$
7–4	7.05	1.00–1.03	1.63	2.03
15–5	5.07	1.58–1.67	1.93	2.03
9–3	2.51	3.36–3.58	3.05	2.02
3–5	1.66	5.80–6.20	4.34	1.97
11–9	1.15	≈9.3	5.65	1.95
8–6	0.80	≈14.	≈7.61	≈1.93

After the scattered wave is calculated in the "spherical" space it must be transformed to the original space. The incoming and scattered fluxes are then compared to give the differential cross section which is integrated together with a $(1-\cos\theta)$ factor to give the scattering cross section σ which in turn gives the relaxation time tensor τ_i from the usual formula

$$\tau_i = 1/nv_i\sigma_i\,,$$

where the relaxation-time tensor[22] has the same principle directions as the mass tensor, and v_i is the velocity of the incoming wave in the ith direction. The cross section σ_i depends on both the energy of the carrier and the direction i. For the case of degenerate statistics these values are taken at the Fermi energy. Combining the masses and relaxation times yields the resistivity for unstrained heavily doped germanium at $T=0$ to be

$$\rho_{4\text{-BH}} = 338.5\left[\frac{1}{J_3}+\frac{39.36}{J_1}\right]^{-1} N^{1/3}\epsilon^{-2}\ \text{m}\Omega\ \text{cm}$$

for the Brooks-Herring analysis, where N is the carrier concentration in units of 10^{18} per cm^3, ϵ is the dielectric constant and J_1 and J_3 are integrals defined in Appendix A, Eq. (A17) and were evaluated by numerical integration on an IBM-1620 computer. Similar formulas were derived in the Conwell-Weisskopf case.

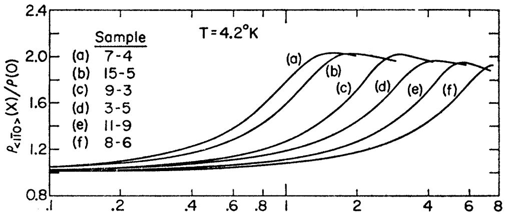

FIG. 24. $\langle 1\bar{1}0\rangle$ resistivity versus stress for arsenic-doped samples. Curves shown are traced from X-Y recorder plots.

In the partial-wave treatment, using Gulyaev's expression for the zeroth-order phase shift[32] (s-wave scattering) we find

$$\rho_{4\text{-G}} = 3.24[1+\cot^2\delta_0(4)]^{-1}N^{-1/3}\ \text{m}\Omega\ \text{cm}\,,$$

where $\cot\delta_0(4)$ is given in Appendix A and N is in units of 10^{18} cm^{-3}. Detailed derivations of $\rho_{4\text{-BH}}$, $\rho_{4\text{-CW}}$, and $\rho_{4\text{-G}}$ are given in Appendix A. The calculated resistivities are plotted in Fig. 3 assuming a dielectric

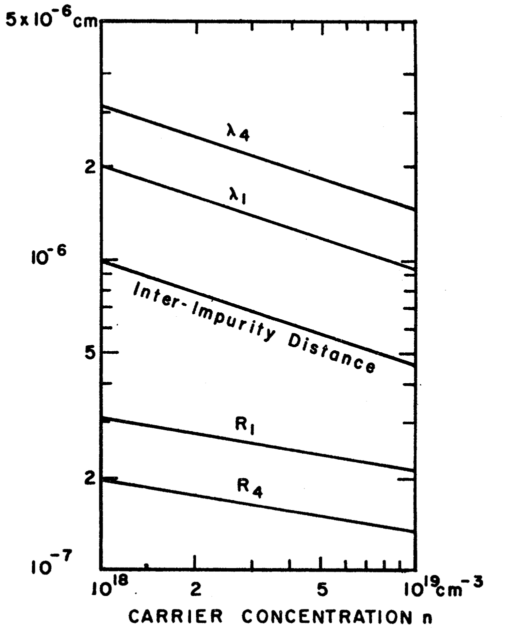

FIG. 25. Calculated values for the averaged de Broglie wavelength λ and Fermi-Thomas screening length R at 0°K, for the one- and four-valley cases, versus carrier concentration.

---

[31] M. C. Gutzwiller (private communication).

[32] Equation (3.2) of Ref. 30.

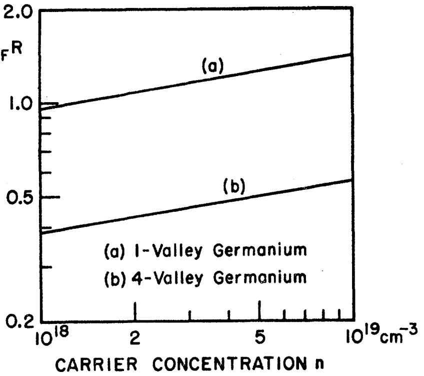

FIG. 26. The product of the magnitude of the wave vector at the Fermi level with the Fermi-Thomas screening length versus carrier concentration in the one- and four-valley cases.

constant of 16.[2] The models give resistivity values of the same order of magnitude as, but less than, the experimental results. The n dependence of the s-wave scattering model resembles that of the data more closely than the Born-approximation model though the numerical agreement is better for the Born approximation. If we take the range of the scattering potential to be the Fermi-Thomas scattering length, the product ka at $T=0$ goes from 0.38 to 0.63 (see Fig. 26). We would then expect the s-wave scattering model to give a more realistic energy dependence than the other models, were an independent scatterer model valid. On the other hand, Csavinszky[29] has shown that extending the partial-wave treatment to the next order reduces the calculated resistivity, bringing it further away from the experimental value.

If we modify our model to include scattering involving clusters of more than one center, resistivity calculated with the independent scatterer model will be increased. Suppose only clusters of m centers are present. The effective number of scatters is reduced by a factor of m while the effective cross section is increased by m^2, the total effect increasing the resistivity by a factor m. To bring the model into agreement with the data m would have to have values between 5 and 10.

The above models do not differentiate between the resistivities in arsenic- and antimony-doped material. However, the difference in core potentials causes a difference in intervalley scattering time[13] which contributes to the resistivity difference of arsenic and antimony doped material.

The intervalley scattering time depends on the matrix element[33]

$$M_{ij}=\int e^{-i\mathbf{k}_i\cdot\mathbf{r}}V(\mathbf{r})e^{+i\mathbf{k}_j\cdot\mathbf{r}}d\mathbf{r},$$

where $V(\mathbf{r})$ is the scattering potential and $\mathbf{k}_i$ and $\mathbf{k}_j$ are wave vectors appropriate to the ith and jth valleys. Then M_{ij} is the Fourier component of the scattering potential with wave number $|k_i-k_j|=1.1\times10^8$ cm^{-1}. The major contribution to this component comes from $R\leq1.5$ Å, which is the size of the core. Therefore, the major contributions to intervalley scattering will be due to the impurity core.

The intervalley scattering relaxation time for heavily doped n-type germanium with arsenic or antimony dopants has been measured by Mason and Bateman.[13] They found that for $n>10^{18}$ Sb per cm^3, $\tau_{\text{intervalley}}$ was $\approx4\times10^{-11}$ sec, while that for arsenic it was 4×10^{-13} sec at 10^{18} dopants per cm^3 decreasing and leveling off to 2.3×10^{-13} sec at 3×10^{19} per cm^3.

If we include anisotropic scattering (see Appendix A), the resistivity ρ_4 in unstrained material is given by

$$\rho_4^{-1}=ne\mu_3[(2K+1)/3],$$

where $\mu_3=e\tau_3/m_3$ is the mobility in the longitudinal direction and K is the mobility anisotropy, i.e., $K=\mu_1/\mu_3$, where μ_1 is the transverse mobility. $K\approx5$ from piezoresistance measurements. Using the resistivity data for antimony doping at 1×10^{18} per cm^3, we find $\tau_3\approx3\times10^{-13}$ sec$\ll\tau_{\text{intervalley}}$. The intervalley scattering is, therefore, negligible in the antimony case. This is not so for arsenic doping.

Before including intervalley scattering in our model, the question of whether or not the impurity core potential that gives rise to the intervalley scattering also contributes to the resistivity by causing an intravalley scattering must be considered. The matrix element M_{ij} that gives rise to intervalley scattering is the same[33] as the matrix element[34] Δ that gives rise to the singlet-triplet energy splitting 4Δ of the ground-state impurity levels in lightly doped Ge. The matrix element M_{ii}, which would give rise to intravalley scattering due to the impurity core, is the same as[34] Λ,

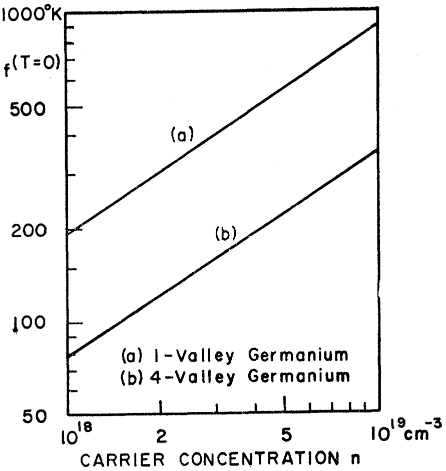

FIG. 27. Degeneracy temperature versus carrier concentration.

---

[33] This is a simplification of Eq. (4) of P. J. Price and R. L. Hartman, J. Phys. Chem. Solids **25**, 567 (1964).

[34] J. H. Reuszer and P. Fisher, Phys. Rev. **135**, A1125 (1964).

the correction to the effective-mass value[35] of the center of gravity of the lowest energy states. The ratio of the intravalley scattering time due to the core to the intervalley scattering time is then

$$\frac{\tau_{\text{intravalley-core}}}{\tau_{\text{intervalley}}}=3\left(\frac{\Delta}{\Lambda}\right)^2, \qquad (2)$$

where the factor 3 comes from the fact that there are three times the density of final states for intervalley scattering than for intravalley scattering. Given the measured[13] intervalley relaxation time and the matrix elements[36,37] Δ and Λ, we may calculate $\tau_{\text{intervalley-core}}$. The appropriate values are: for Sb, $\Lambda=0.7\pm2$, $\Delta=0.08\pm0.01$, and for As, $\Lambda=0.2\pm0.2$, $\Delta=1.06$, in units of meV.

Applying Eq. (2), we find that the intravalley scattering due to interactions with the impurity core may be neglected for As doping by not for Sb doping. Starting with the total relaxation time for Sb scatterers, removing the intravalley impurity core scattering, and adding the intervalley scattering for As doping, we may predict a resistivity ratio $\rho_{\text{Sb}}/\rho_{\text{As}}$ if we assume the relaxation times add strictly as[27] $\tau^{-1}=\sum_i \tau_i^{-1}$. At 10^{18} and 10^{19} concentrations the values of $\rho_{\text{Sb}}/\rho_{\text{As}}$ thus calculated are 0.94 and 0.85, respectively, while the experimental values are 0.68 and 0.57. We have shown, in qualitative agreement with experiment, that intervalley scattering increases the resistivity of As-doped material over that doped with Sb and that the resistivity ratio increases as doping increases from 10^{18} to 10^{19} dopants per cm^3. A more complete discussion should include the increase of the mobility ratio $\mu_{\text{Sb}}/\mu_{\text{As}}$ with increasing carrier concentration due[38] to the change of the Thomas-Fermi screening but our present knowledge does not warrant this.

Morimoto and Tani[39] have proposed that the interference of the strain scattering, due to impurities having atomic radii different from those of the host atoms, with the Coulomb scattering due to the screened ionized impurities can explain the difference between the resistivities of As- and Sb-doped germanium. Applying their model to our case, we found that this effect is negligible in degenerate semiconductors at low temperatures.

B. Resistivity of Saturated Material: Dependence on Carrier Concentration at 4.2°K

Since in the saturated case all carriers are in one valley, for a given impurity concentration the degeneracy temperature is $4^{2/3}$ times the value in the unstrained case. It is, therefore, even more appropriate to assume complete Fermi degeneracy at 4.2°K in the saturated case.

As in the unstrained case, it is possible to calculate resistivity according to the Brooks-Herring, Conwell-Weisskopf, and Gulyaev models. The formulas for ρ_3 and ρ_1 derived from these models are given in Appendix A; results are plotted in Figs. 4 and 5.

As in the case for unstrained material the Brooks-Herring model predicts resistivities closer to the measured values than those predicted by the other models, however, the n dependence is more closely given by the Gulyaev model.

Contrary to the four-valley case, we may no longer use the intervalley scattering to explain the higher resistivity in arsenic-doped material than in that doped with antimony at a given carrier concentration. In fact, following the discussion of the previous section and using the data of Mason and Bateman[13] and that of Reuszer and Fisher[34] to compute intravalley scattering due to that part of the core potential that causes intervalley scattering, one finds that in all cases the intravalley scattering time for arsenic is greater than for antimony. This predicts a greater resistivity for the antimony case in disagreement with the data. To explain the greater resistivity in the arsenic-doped one-valley material on an independent-scattering model, we may only use the qualitative argument of Csavinszky[38] that the deeper core potential in arsenic must somehow yield a lower mobility.

C. Resistivity Dependence on Temperature

The temperature dependence of the resistivity of unstrained material has been a subject of speculation for some time.[3,40,41] Though an increase in resistivity due to enhanced lattice scattering for increasing temperature is expected, this can account for but a small part of the observed increment.

The contribution of lattice scattering in degenerate materials may be determined from that in "pure" materials as follows: The lattice scattering relaxation time varies with the inverse of the square root of the carrier energy[42] which for pure material introduces a factor of the $\sqrt{T}$ into the denominator of the mobility.

---

[35] W. Kohn, *Solid-State Physics*, edited by F. Seitz and D. Turnbull (Academic Press Inc., New York, 1957), Vol. 5, p. 257.

[36] Λ may be determined either from purely optical data (Ref. 34) or by using an optically determined Δ and a value for the ground-state ionization energy determined from the temperature dependence of Hall coefficient (Ref. 25). These two methods yield the same results in the Sb case, but in the As case the purely optical method yields a value of Λ much larger than that given by the other case. The latter Λ is appropriate to our case, the large value in the optical case presumably being due to the Franck-Condon principle.

The value of Δ for Sb given by Reuszer and Fisher (Ref. 34), $\Delta=0.08$ meV does not agree with that of Fritzsche (Ref. 37) $\Delta=0.14$ meV. We chose to use the 0.08 value because it satisfies the intervalley scattering-time data when used in the formula $\tau_{\text{i.v.Sb}}/\tau_{\text{i.v.As}}=\Delta_{\text{As}}/\Delta_{\text{Sb}}^2$.

[37] H. Fritzsche, Phys. Rev. **120**, 1120 (1960).

[38] P. Csavinszky, J. Phys. Soc. Japan **16**, 1865 (1961).

[39] T. Morimoto and K. Tani, J. Phys. Soc. Japan **17**, 1121 (1962).

[40] T. N. Morgan, Bull. Am. Phys. Soc. **8**, 224 (1963).

[41] D. Long, J. D. Zook, P. W. Chapman, and O. N. Tufte, Solid State Communications **2**, 191 (1964).

[42] Cf., Ref. 2, p. 146.

TABLE VII. Values of the slope of the resistivity-versus-stress curves in the range of linear behavior.

Antimony doping Sample	 $\frac{\Delta\rho_L}{\rho X}$ $(10^{-4}\ \mathrm{cm^2/kg})$	Arsenic doping Sample	 $\frac{\Delta\rho_L}{\rho X}$ $(10^{-4}\ \mathrm{cm^2/kg})$
12–1	−8.6	15–1	−5.3
13–1	−6.3	10–3	−2.6
14–1	−3.0	3–4	−2.3
5–4	−2.4	11–5	−1.4
6–10	−1.5	8–5	−1.3
	$\frac{\Delta\rho_{(1\bar{1}0)}}{\rho X}$ $(10^{-4}\ \mathrm{cm^2/kg})$		$\frac{\Delta\rho_{(1\bar{1}0)}}{\rho X}$ $(10^{-4}\ \mathrm{cm^2/kg})$
12–4	−6.6	7–4	−6.1
13–3	−5.9	15–5	−4.7
14–3	−2.5	9–3	−2.1
5–5	−1.6	11–9	−1.6
6–12	−1.3	8–6	−0.8

This must be modified for degenerate material. So long as the ambient temperature is small as compared to the degeneracy temperature the carrier energy may be taken as the Fermi energy. The above shows that

$$\mu_{\text{latt. deg.}}=(\tfrac{3}{2}\times T/T_D)^{1/2}\mu_{\text{latt. pure}}. \tag{3}$$

The lattice mobility for pure material has been measured at low temperatures by many authors. Using the data of Koenig *et al.*[25] and Eq. (3), it is easily shown that, in the first place, at liquid-helium temperature the lattice scattering contribution to the resistivity is less than 0.3% for all concentrations considered—hence negligible, and secondly, at $T=0.3\ T_D$ the contribution is less than 5% for even the worst case (highest doping) and cannot account for the observed values of about 13 to 15% (Figs. 6 and 7).

Mansfield[43] has derived the temperature dependence of conductivity due to screened ionized impurity scattering in the case of a spherical effective mass m^* to be

$$\sigma_I=\frac{32\epsilon^2 m^*(kT)^3 f_2(\eta^*)}{Ne^2h^3f(x)},$$

where

$$f(x)=\ln(1+x)-x/(1+x)$$

and

$$x=\frac{\bar{\eta}(kT)^{1/2}\epsilon h}{e^2(2m^*)^{1/2}f_{1/2}'(\eta^*)},$$

where $\bar{\eta}$ satisfies

$$(\bar{\eta}-3)\exp(\bar{\eta}-\eta^*)=\bar{\eta}+3.$$

N is the concentration of scattering centers, ϵ is the dielectric constant, η^* is the reduced Fermi energy and f_2 and $f_{1/2}$ are Fermi integrals, defined in the usual way.[44] The temperature dependence here calculated comes from the temperature dependence of the screening length and the kT spread about the Fermi surface. The four-valley nature of the germanium case can be accounted for by dividing the x function by 4, but the mass and scattering anisotropies are not easily incorporated into this model.

Using the density-of-states mass for the conduction band of pure germanium, $\Delta\rho_4(T)/\rho_4(0)$ may be calculated. The results of this calculation are given in Table IX. It is seen that though for lower dopings the temperature dependence of screened ionized impurity scattering contributes significantly to the observed increase in resistivity, it does not explain the large effect in the more highly doped material.

It has been proposed by Morgan[40] that interband carrier-carrier scattering is significant in degenerate semiconductors and could account for the otherwise unexpected large increase of resistivity with temperature at low temperatures. It is shown in Appendix B that carrier-carrier interactions may be significant in the four-valley case but they can have little or no effect on the one-valley case. This is consistent with the measurements as no increase of resistivity with temperature is ever measured in the one-valley case.

Koenig[3] has suggested a mechanism to give a positive temperature coefficient at low temperature due to scattering by a dipole created by the inability of the electron cloud to follow the thermal vibrations of the ionized impurity. Though this mechanism yields the appropriate temperature dependence in the four-valley case it predicts similar behavior in the one-valley case; this is not observed.

The data of Figs. 6 and 7 show a hump in the $\rho_4(T)$ curves for the samples with lowest impurity concentrations. None of the above-mentioned mechanisms predict such a dependence. In Appendix A it is pointed out that the method of calculating the total scattering cross section depends significantly on the product ka, where k is the carrier wave number and a is the screening length of the scattering potential. If $ka\gg1$, the Born approximation is valid and the Brooks-Herring and Conwell-Weisskopf treatments are appropriate within the spirit of the independent particle approximation. The Mansfield model discussed above is based on this

TABLE VIII. Change in resistivity in longitudinal samples in various states of strain on application of a transverse magnetic field.

Sample	X/X_{sat}	$[\rho_L(H)-\rho_L(0)]/\rho_L(0)\,\vert_{H=10\text{ kG}}$
7–3	0.0	−0.001±0.003
	0.9	−0.007±0.003
	1.7	−0.011±0.003
5–4	0.0	0.000±0.003
	1.0	−0.006±0.003
3–4	0.0	−0.001±0.003
	1.0	−0.005±0.003

---

[43] R. Mansfield, Proc. Phys. Soc. (London) **B69**, 76 (1956).

[44] Cf., J. McDougall and E. C. Stoner, Phil. Trans. Roy. Soc. **A237**, 67 (1938).

TABLE IX. $\Delta\rho_4(T)/\rho_4(0)$ calculated according to Mansfield (Ref. 43).

n	$T=0.1T_D$	$T=0.3T_D$
1×10^{18}	0.05	0.15
5×10^{18}	0.00	0.05
10×10^{18}	0.00	0.02

assumption. If $ka\ll1$ the s-wave scattering cross section is valid and the Gulyaev treatment is appropriate. From Fig. 26 it is clear that neither extreme case is strictly satisfied in the cases that concern us, however, the lowest ka in the region of interest is for the four-valley case of the samples with least impurity concentrations. Using the s-wave scattering treatment of Gulyaev, Long *et al.*[41] have shown that a resonance scattering mechanism is predicted that yields a hump in the temperature dependence of the resistivity and to that extent it is possible to interpret the measured temperature dependence in the $n\approx1\times10^{18}/\text{cm}^3$ samples to be due to resonance scattering. [*Note added in proof.* The results of more accurate measurements of the T dependence in unstrained samples and their implications are discussed in a forthcoming communication by M. J. Katz, S. H. Koenig, and A. A. Lopez.]

At stresses so high and temperatures so low that the edge of the upper three valleys is more than a number of kT above the Fermi level the conduction band of the material can be considered to be a single valley because no carriers will be in the higher valleys.

As shown in Appendix B, electron-electron scattering cannot affect the resistivity in this case. It remains to examine the temperature dependence of resistivity predicted by Mansfield's equation. Results of this calculation of $\rho(T)/\rho(0)$ are given in Table X, together with the measured values. There is agreement in the sense that the model predicts a reduction of resistivity of some percent, monotonic over the temperature range considered. On the other hand, the model predicts a lower resistivity ratio for higher doping at a given T/T_D and, in fact, the data show the opposite. This is because we have left out the effect of lattice scattering. At a given T/T_D the material with higher T_D will have a larger contribution of lattice scattering which raises the resistivity above that of the lower doped sample. The lattice contribution may be calculated from the data of Koenig *et al.*[25] by using Eq. (3). This technique gives very good results when comparing the $\rho_1(T)$ data for 1×10^{18} and 3.34×10^{18} Sb per cc, where such a calculation predicts an increase of 1% in the resistivity ratio for the more highly doped material at $T=0.1T_D$.

To understand the $\rho(T)$ behavior for a given sample at various post saturation stresses we argue as follows: the common curve for the higher stresses gives the true $\rho(T)$ behavior for the one-valley case. The lower stress curves diverge from the one-valley curve when a sufficient number of carriers are excited into the upper valleys; the lower the applied stress the lower the T/T_D at which this effect begins to contribute. In the ρ_3 case the resistivity is being measured in the low mobility direction of the lowest valley and exciting carriers to the upper valleys allows a contribution from the higher mobility directions and reduces the resistivity. In the ρ_1 case the opposite is true and the resistivity is increased.

In analyzing the data of Figs. 13 and 14, we find that, while the argument given above is qualitatively correct using the mobility anisotropies determined from the piezoresistance data, it is necessary that the mobilities in the upper valleys be approximately the same as those in the lowest valley. At low temperatures the kinetic energy of the carriers in higher valleys is significantly lower than that of those in the lowest valley and, reasoning from Rutherford scattering, we might expect them to have a lower mobility. On the other hand, the number of carriers excited to the higher valleys is very small so that the screening will still be determined by the carriers in the lowest valley alone. In the case of the low carrier energy this screening length will dominate the scattering cross section (see Appendix B) and consequently the mobilities in the upper valley will be closer to those of the lowest valley than otherwise expected.

D. Piezoresistance Experiments

(*a*) *Initial Stress Dependence*

The results of the various piezoresistance experiments described in Sec. III. E, F, and G can be understood qualitatively in terms of the piezoresistance tensor[45] and the deformation potential model.[46] Following Smith's[45] notation it is easily shown that application of a small stress X in a $\langle111\rangle$ direction in a cubic crystal results in a linear change in the resistivity parallel to that direction given by

$$\delta\rho_L/\rho X=\tfrac{1}{3}[\Pi_{11}+2\Pi_{12}+2\Pi_{44}], \tag{4}$$

where ρ_L corresponds to the resistivity measured in our longitudinal samples and Π_{ij} are the components of the piezoresistance tensor. Similarly it may be shown that

$$\delta\rho_T/\rho X=\tfrac{1}{3}[\Pi_{11}+2\Pi_{12}-\Pi_{44}]. \tag{5}$$

For the stress applied in a $\langle1\bar{1}0\rangle$ direction the approp-

TABLE X. $\rho(T)/\rho(0)$ in the one-valley case calculated according to Mansfield (Ref. 43) compared with measured values for longitudinal samples.

	Theory		Experiment	
n	$T=0.1T_D$	$T=0.3T_D$	$T=0.1T_D$	$T=0.3T_D$
1×10^{18}	0.97	0.87	≈0.93	<0.8
5×10^{18}	0.97	0.82	≈0.98	≈0.88
10×10^{18}	0.96	0.77		

---

[45] C. S. Smith, Phys. Rev. **94**, 42 (1954).

[46] Cf., R. W. Keyes in Ref. 35, Vol. II, p. 149 (1960).

riate relation is

$$\delta\rho_{\langle 1\bar{1}0\rangle}/\rho X = \tfrac{1}{2}[\Pi_{11}+\Pi_{12}+\Pi_{44}]. \tag{6}$$

The above depends on cubic symmetry only and is true for any cubic crystal.

To calculate values for the piezoresistance tensor components and thereby to predict the results of resistivity measurements, it is necessary to assume a model for the band structure of the material in question and its transport properties which includes the affects of strain.

Since the material in question is heavily doped *n*-type we need only concern ourselves with the nature of the conduction band. In the pure material the conduction band edge is well known.[2] We will take as our model for the conduction band of degenerate germanium the set of four valleys appropriate to the pure material with the density of states determined by the pure material effective mass. This model has a sharp conduction band edge. We expect to detect any deviation from this model, e.g., tailing of the band edge, from our experiments.

As we have seen above and in Appendices A and B, any even fairly reasonable picture of the scattering mechanism in degenerate material must depend on the screening length and be a complicated function of the carrier energy. Transport equations are further complicated by the anisotropic mass tensor of the germanium valleys. In order to simplify the model for the transport mechanism we will let the mobility tensor components for a given valley, $\mu_{\parallel}$ along its axis of rotation and $\mu_{\perp}$ perpendicular to it, be independent of energy. (The symmetry of the crystal demands that the mobility tensor be an ellipsoid of revolution.) Comparing Figs. 4 and 5, we see that all of the models discussed would predict $\mu_{\perp} > \mu_{\parallel}$.

To describe the affect of strain on the conduction band we will use the deformation potential model and assume that valley motion due to strain is the same as that in the pure case. For a compressional stress X applied in a $\langle 111\rangle$ direction the valley associated with that direction moves down in energy while the other three move up together. The energy split between the edge of the lowest valley and that of the other three is given by[47]

$$\Delta E_{\langle 111\rangle} = -(4/9)(\Xi_u/C_{44})X_{\langle 111\rangle}, \tag{7}$$

where C_{44} is an elastic stiffness constant, Ξ_u the deformation potential is positive and ΔE is positive for compressional (negative) X.

For the case of stress applied in a $\langle 1\bar{1}0\rangle$ direction two valleys are raised and two lowered and the energy split between the respective band edges is easily calculated to be

$$\Delta E_{\langle 1\bar{1}0\rangle} = -\tfrac{1}{3}(\Xi_u/C_{44})X_{\langle 1\bar{1}0\rangle}. \tag{8}$$

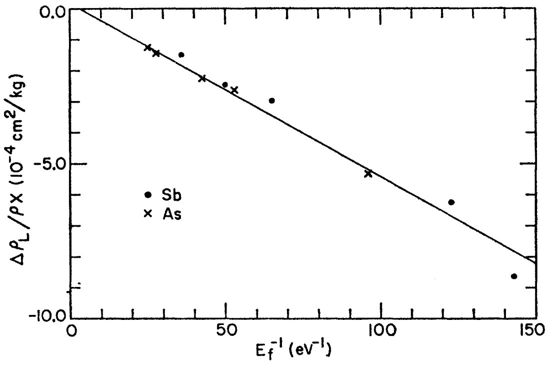

FIG. 28. $\Delta\rho_L/\rho X$ versus reciprocal Fermi energy, in the linear range.

In the case of stress applied in a $\langle 100\rangle$ direction the deformation potential model yields no separation of valleys, the motion being the same for all four. Therefore, as far as our model is concerned their will be no change in resistivity for such an applied stress. Smith[45] in his contact arrangements A and B has shown that piezoresistance components Π_{11} and Π_{12} are proportional to changes in resistivity components due to an applied stress in the $\langle 100\rangle$ direction, therefore, for our model we may conclude that

$$\Pi_{11} = \Pi_{12} = 0$$

and that Eqs. (4), (5), and (6) reduce to

$$\delta\rho_L/\rho X = \tfrac{2}{3}\Pi_{44};\quad \delta\rho_T/\rho X = -\tfrac{1}{3}\Pi_{44}$$

and

$$\delta\rho_{\langle 1\bar{1}0\rangle}/\rho X = \Pi_{44}/2. \tag{9}$$

Therefore, we predict that

$$\frac{\delta\rho_{\langle 1\bar{1}0\rangle}}{\rho X}\bigg/\frac{\delta\rho_L}{\rho X} = 0.75.$$

Comparing the longitudinal and $\langle 1\bar{1}0\rangle$ data of Table VII, we find experimental values of the ratio to be between 0.65 and 0.85, in agreement with the model to within the experimental error. Though the magnitude of the piezoresistance in the transverse case could not be accurately measured it is opposite in sign to the others and extrapolation of the ρ_T data shows it to agree with the model to within a factor of 2.

Application of stress and the consequent shifting of valleys causes a change in the resistivity for two reasons. The redistribution of electrons from higher to lower valleys changes their effective mobility because the mobility (1) is anisotropic and (2) depends on carrier velocity in general. If we assume the mobility anisotropy $K = \mu_{\perp}/\mu_{\parallel}$ to be constant and the intrinsic velocity dependence to vary as v^J [see Eq. (1)] the model yields

$$\frac{\delta\rho_{\langle 111\rangle}}{\rho X} = -\frac{1}{9}\frac{\Xi_u}{c_{44}E_f}(J+3)\frac{K-1}{2K+1} \tag{10}$$

---

[47] Equation (7) may be derived from Ref. 18, Eq. (C6). Details of the derivation are given in Ref. 17.

for degenerate statistics. E_f is the Fermi level in the four-valley case. For J we will take the value determined from Eq. (1) for the four-valley case, viz., $J \approx 2.7$. Values[34,48–50] for Ξ_u reported in the literature vary from ≈ 16 to ≈ 20 eV.

Plotting $\Delta\rho_L/\rho X$ versus E_f^{-1} (see Fig. 28) and measuring the slope we calculate values for K between 3.2 and 18 because of the large uncertainty of Ξ_u and the strong dependence of K on the slope. If we choose the higher value of Ξ_u, we get K in the range 3.2 to 4.9. In any event, the initial independence of ρ on stress is of proper sign and reasonable magnitude in all three types of piezoresistance experiments.

The initial stress dependence of the Hall coefficient is similarly explained. Using the same model but neglecting the explicit energy dependence of mobility we get the following formula for the Hall coefficient:

$$R_H = -\frac{1}{e}\frac{K[n_{\rm I}+n_{\rm II}(5/9+4K/9)]}{[n_{\rm I}+n_{\rm II}(1/9+8K/9)][n_{\rm I}K+n_{\rm II}(5K/9+4/9)]}, \tag{11}$$

where $n_{\rm I}$ is the carrier concentration in the lowest valley and $n_{\rm II}$ is the total carrier concentration in the three upper valleys. In the unstrained case $n_{\rm I}=\frac{1}{4}n$, $n_{\rm II}=\frac{3}{4}n$, and Eq. (11) reduces to

$$R_H = -\frac{1}{ne}\frac{3(2+K)}{(1+2K)^2} \tag{12a}$$

in agreement with Herring's[18] formula. In the saturated conditions $n_{\rm I}=n$, $n_{\rm II}=0$ and Eq. (11) reduces to

$$R_H = 1/ne \tag{12b}$$

as discussed in Sec. III A. For a compressional stress in the $\langle 111\rangle$ direction $n_{\rm I}$ increases and $n_{\rm II}$ decreases (their sum remaining constant) such that for typical values of K, R_H shows an initial decrease for slight population shifts, in agreement with the data in Figs. 16 and 21.

(b) *High-Stress Dependence of Resistivity in Antimony-Doped Samples*

If we attempt to evaluate the high-stress data in terms of the model that includes only the velocity dependence of the mobility (and neglects intervalley scattering) we predict a final resistivity ratio of

$$[(2K+1)/3]4^{-J/3} \tag{13}$$

in the longitudinal case. If we use this expression to determine K from the data, we get values of 20–30—much larger than those determined by the more accurate methods used below. Though the model including J is satisfactory, in fact necessary, in explaining the linear piezoresistance data it would appear to be inappropriate to the present case. In the case of linear piezoresistance small changes in the energy of some carriers are involved and significant changes of the screening length are not anticipated. Under such conditions we must use the J dependence. In the case of high stress and large population shifts between valleys, the carrier energy and screening length change drastically thereby changing the scattering picture in a complicated way (see the discussion below). Under these conditions the model must be augmented to include the dependence of the screening length on the relative valley populations, the effect of which tends to nullify the effect of including J.

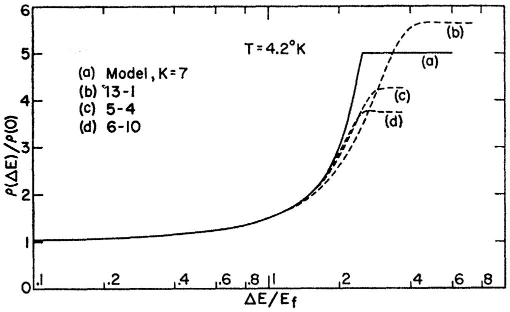

FIG. 29. Calculated resistivity ratio versus energy splitting [curve (a)] together with data shifted horizontally to show the fit to Eq. (14) (cf., associated discussion).

Empirically, we have found it a better approximation to take a constant K and energy independent mobilities although even this model needs modification in the ρ_T and $\rho_{\langle 1\bar{1}0\rangle}$ cases. Using the model of constant K, and energy-independent mobilities, and still neglecting intervalley scattering, we derive the equation

$$\frac{\rho_L(X)}{\rho(0)} = \frac{2K+1}{3}\left[1+\frac{n_{\rm II}(X)}{n}\frac{8}{9}(K-1)\right]^{-1} \tag{14}$$

for the longitudinal case, where $n_{\rm II}/n$ is the fraction of carriers remaining in the upper valleys. The parabolicity of the density of states curve requires that $n_{\rm II}/n$ satisfy

$$\frac{\Delta E}{E_f} = 4^{2/3}\left[\left(1-\frac{n_{\rm II}}{n}\right)^{2/3} - \left(\frac{n_{\rm II}}{3n}\right)^{2/3}\right], \tag{15}$$

where E_f is the Fermi level for unstrained material and ΔE the energy splitting between the lowest and upper three valleys is given by Eq. (7).

If Eq. (14) is plotted versus ΔE, i.e., linear with stress, for various values of K it turns out that except for the fact that curves for lower values of K cut off, i.e., saturate, at lower final resistivity ratios, all such curves have the same shape and may be brought into congruence by adjusting the scale ΔE. The "shape" of these curves is independent of K and determined by the parabolicity of the density of states. In Fig. 29 we

---

[48] H. Fritzsche, Phys. Rev. **115**, 336 (1959).

[49] R. Ito, H. Kawamura, and M. Fukai, Phys. Letters **13**, 26 (1964).

[50] J. J. Hall, Phys. Rev. **137**, A960 (1965).

TABLE XI. The mobility anisotropy as determined from longitudinal- and transverse-resistivity measurements on one-valley antimony-doped samples.

$n(10^{18}\ \mathrm{cm}^{-3})$	$K=\dfrac{\rho_L(\mathrm{sat})}{\rho_T(\mathrm{sat})}$
1.10	5.5±0.2
1.36	4.9±0.2
3.54	4.6±0.2
5.15	3.6±0.2
9.14	3.8±0.2

plot $\rho_L/\rho(0)$ versus $\Delta E/E_f$ for several antimony-doped samples. The abscissas are shifted to coincide with the plot of Eq. (14) for $K=7$. Good agreement is evident at low strain and is maintained until deviations from parabolicity and inhomogeneity of the sample begin to affect the shape of the curve.

Equation (14) predicts a final resistivity ratio of $(2K+1)/3$. Using this formula to calculate K from the antimony data we find K varies monotonically from 8.5 at 1.1×10^{18} carriers per cm^3 to 5.2 at 8.5×10^{18}. For the arsenic-doped material K is in the range 9.5 at 1.2×10^{18} to 7.5 at 6.5×10^{18}. There is no correction for intervalley scattering in the antimony case; for the arsenic case, the K values would be increased ~15%.

The above determination of the mobility anisotropy is highly approximate in that it makes no allowance for the change of mobility with carrier energy or scatterer screening length. To obtain the best value of K for screened ionized impurity scattering, we should simply compare $\rho_L(\mathrm{sat})$ and $\rho_T(\mathrm{sat})$ for antimony-doped material. In the saturated condition, where neither electron-electron nor intervalley scattering can contribute, the mobility components may be measured individually and at comparable Fermi levels. Interpolating the $\rho_T(\mathrm{sat})$ data to Fermi levels appropriate to the $\rho_L(\mathrm{sat})$ data we find K from

$$K=\rho_L(\mathrm{sat})/\rho_T(\mathrm{sat})\,. \tag{16}$$

The results, given in Table XI, show that K decreases from 5.5 at 1.1×10^{18} to 3.8 at 9.1×10^{18} carriers per cm^3. The modified Gulyaev model described in Appendix A gives values of $\rho_L(\mathrm{sat})/\rho_T(\mathrm{sat})$ decreasing from 7.9 at 1×10^{18} to 3.4 at 10×10^{18}. The modified Brooks-Herring treatment yields $\rho_L(\mathrm{sat})/\rho_T(\mathrm{sat})$ values decreasing by a factor of $\frac{3}{4}$ over this range but the values are about an order of magnitude higher than those measured.

If we want to modify our model to include the mobility dependence on energy and screening length, we use the two equations in Appendix B. For example, if we use the values of Fig. 25 in Eq. (B1) and then calculate the mobility anisotropy from the $\rho_L(\mathrm{sat})/\rho(0)$ data we find $K=2.4$ for $n=1\times10^{18}\ \mathrm{cm}^{-3}$. Recalling the values obtained when the J dependence alone was included (20–30) we find that including the screening effect may reduce the anisotropy by a factor of 10. The true value, from $\rho_L(\mathrm{sat})/\rho_T(\mathrm{sat})$, is found to be in between the extreme cases.

An equation for $\rho_T(X)/\rho(0)$ may be derived for our model along the lines of Eq. (14). This treatment predicts a final resistivity ratio of $(2K+1)/3K$ which for any reasonable K is less than 1, a condition not satisfied by the data for antimony-doped material. The reason for this is that as stated above the energy and screening length dependence must be included. When this is done the measured final transverse resistivity ratios are consistent with the other data.

The simple model predicts a final resistivity ratio of $(2K+1)/(2+K)$ for the $\langle 1\bar{1}0\rangle$ data. As in the longitudinal case the measured final resistivity ratio is higher, by a similar amount, because of the energy and screening length dependence of the scattering mechanism.

The Hall coefficient measurements also yield a value for K calculated from the ratio of Eq. (12a) to Eq. (12b). The value for K thus obtained from the data for antimony-doped material is 5±1 the large error due to the weak dependence of Eq. (12a) on K and the poor accuracy of the Hall coefficient measurements.

(c) *Energy Shift ΔE and Saturation*

Using Eq. (7) and the parabolic density-of-states model it is possible to predict a value for saturation stress depending on Ξ_u. The positions of all but the lowest experimental saturation stresses for antimony-doped samples lie at points between those predicted by the highest and lowest Ξ_u values reported and no conclusion can be drawn except that at low dopings the conduction-band edge is probably less sharp than in more heavily doped material.

The arsenic-doped material, on the other hand, shows a late saturation for all concentrations and agrees with the lightest doped antimony sample. It appears as if a Ξ_u of 15 eV or less were appropriate in the arsenic case.

(d) *High-Stress Dependence of Resistivity in Arsenic-Doped Samples*

In all resistivity versus stress data taken for arsenic-doped samples a peak in the resistivity occurred. In the longitudinal case the peak was about 20% higher than the final resistivity and occurred at a stress about 20% less than the saturation stress. In the transverse case the peak was 5–10% higher than the final value. In addition, the longitudinal resistivity did not cease changing at X_{sat} but continued decreasing for stresses up to 2 and 3 times the saturation value. Since intervalley scattering is very large in arsenic-doped material we qualitatively interpret the peaking effect as follows: Throughout the resistivity-versus-stress curve the intervalley scattering contributes significantly to the resistivity. A maximum in the resistivity will occur at a stress near but below saturation when the increase in resistivity due to transfer of carriers to the lowest valley becomes less important than the decrease in the density of final states in the upper three valleys to which carriers may be scattered by the intervalley scattering mechanism. When saturation is reached the upper three valleys are depopulated and the Hall coefficient stops changing. If there are states below the conduction band edge[51] that are accessible to intervalley scattering but which may not be sufficiently occupied so that raising them above the Fermi level does not change the Hall coefficient, then the resistivity will continue to decrease at stresses above X_{sat}, until no more such "tail" states are available. The length of the tail below the conduction band edge as determined by X_{final} is from 0.03 to 0.04 eV.

The existence of states that may be available for intervalley scattering though not contribute to the Hall effect may be understood by considering the case of the lattice with one donor. The donor introduces an available state under each of the conduction band valleys, however, if one of those states is occupied the others may not be, i.e., the possibility of occupying a given state depends on the occupancy of other states. Realizing that many of the states in the lowest valley are impurity type states it is felt reasonable that occupancy of tail states under the three upper valleys may be contingent on the occupancy of states in the lowest valley though they are still available for intervalley scattering from the lowest valley states. A more precise argument is not available at present.

Small peaks, are also discernable in the longitudinal data for antimony-doped material, ranging from a peak value 1.7% above ρ_{final} for sample 14–1 to peaks on the order of tenths of a percent in other samples. (This is a real effect. The correction due to geometrical strain effects has the opposite sign.) If we consider the additional scattering in the peak over the final resistivity value to be indicative of the strength of intervalley scattering then the ratio of intervalley scattering in our arsenic and antimony samples is of the same order of magnitude as that measured by Mason and Bateman.

(e) *Magnetoresistance*

The negative magnetoresistance in the one-valley case cannot be explained by conventional transport theory. Negative magnetoresistance has also been measured in unstrained material[8,9] but no satisfactory explanation has been given. Our results indicate that the negative magnetoresistance coefficient is from 5 to 10 times larger in the one-valley case than in the unstrained material.

V. SUMMARY

We have shown that independent scatterer models are useful in interpreting the carrier concentration dependence of resistivity in heavily doped n-type germanium even though the assumption of independent scatterers is not appropriate. Electron-electron scattering and the temperature dependence of screening length both contribute to the temperature dependence of resistivity in unstrained material. In the saturated case electron-electron scattering does not affect the resistivity.

The results of all the piezoresistance experiments are qualititively understood in terms of a simple anisotropic scattering model, provided that the energy dependence of mobility and the *variation of the screening* are taken into account. A large effect due to intervalley scattering was found in arsenic-doped samples. The initial stress dependence of the various piezoresistance experiments may be understood in terms of the piezoresistance tensor and deformation potential models.

The mobility anisotropy for scattering in one-valley antimony-doped germanium has been measured and found to vary from 5.5 at 10^{18} to 3.8 at 10^{19} carriers per cm^3. A tailing of the band edge that extends on the order of 0.03 to 0.04 eV into the forbidden energy gap has been found for dopings in the range 10^{18} to 10^{19} per cm^3.

ACKNOWLEDGMENTS

The author would like to thank Dr. Seymour H. Koenig for suggesting this investigation and for continued guidance and encouragement throughout the work; Dr. A. P. Speiser and the staff of the IBM Zurich Research Laboratory, in particular, Dr. H. Thomas and Dr. M. C. Gutzwiller; Don Alberto Lopez for invaluable assistance in sample preparation and data taking and W. Schillinger of the IBM Watson Laboratory for the machine computation. The crystals from which the samples were prepared were very kindly supplied by Dr. Geoffrey Brock of the IBM Thomas J. Watson Research Center.

APPENDIX A

Calculation of the Relaxation Time Tensor for Ellipsoidal Energy Surfaces

The usual discussions of the scattering problem[52] assume spherical energy surfaces at the very outset. For the case of a tensor mass, the wave equation, choosing the Cartesian coordinates in the characteristic directions of the mass tensor, is

$$i\hbar\frac{\partial\Psi}{\partial t}=-\frac{\hbar^2}{2}\left(\frac{1}{m_1}\frac{\partial^2}{\partial x^2}+\frac{1}{m_2}\frac{\partial^2}{\partial y^2}+\frac{1}{m_3}\frac{\partial^2}{\partial z^2}\right)\Psi+V(\mathbf{r},t)\Psi\,.$$

---

[51] Cf., M. Lax and J. C. Phillips, Phys. Rev. **110**, 41 (1958); Cf., also Ref. 4.

[52] Cf., L. I. Schiff, *Quantum Mechanics* (McGraw-Hill Book Company, Inc., New York, 1955), 2nd ed. Chaps. V and VII.

Using the usual definition of the probability current density $\mathbf{S}$,[53]

$$\frac{\partial}{\partial t}\int_V \Psi^*\Psi d\tau = -\oint \mathbf{S}\cdot d\mathbf{A},$$

it is easy to show that in the anisotropic case

$$\mathbf{S}=\frac{\hbar}{2i}[\psi^*\mathbf{O}\psi-\psi\mathbf{O}\psi^*], \tag{A1a}$$

where the operator $\mathbf{O}$ has components

$$\mathbf{O}_i=\frac{1}{m_i}\frac{\partial}{\partial X_i}, \tag{A1b}$$

where $X_i=x$, y, z for $i=1$, 2, 3.

Our aim is to compute the scattering cross section appropriate to the anisotropic case. Since we are interested in energy surfaces that are ellipsoids of revolution (appropriate to the band structure of Ge) we need only consider incoming waves in the transverse (x or y) directions or longitudinal (z) direction to get the entire conductivity tensor. Consider an incoming plane wave in the z direction:

$$\psi_{z,in}=e^{ik_z z},$$

where $E=\hbar^2k_z^2/2m_z$ is the energy of the particle. The incoming current, in the z direction is by Eq. (A1)

$$S_z=\hbar k_z/m_z=(2E/m_z)^{1/2}. \tag{A2}$$

In calculating the scattered flux an outgoing spherical wave of the form

$$\psi_{\text{scatt}}=f(\theta,\varphi)(e^{ikr}/r)$$

is normally assumed, but this may be done only where the energy surfaces are spherical. We may, however, transform to a primed coordinate space in which the energy surfaces are spherical by the transformation

$$X_i'=(m_i/m_d)X_i; \tag{A3}$$

the kinetic energy operator in primed space becomes

$$-(\hbar^2/2m_d)(\nabla')^2$$

and has spherical symmetry. Here $m_d=(m_1m_2m_3)^{1/3}$ is the usual density-of-states mass.

The scattered wave in primed space may then be written

$$\psi_{\text{scatt}}=f(\theta',\varphi')(e^{ik'r'}/r'), \tag{A4}$$

where

$$k'=\left(\frac{2m_dE}{\hbar^2}\right)^{1/2}$$

and θ' and φ' are the inclination and azimuthal, respectively. It is easily shown that

$$\varphi'=\varphi \quad\text{and}\quad \cos\theta'=\frac{\cos\theta}{(m_1/m_3)\sin^2\theta+\cos^2\theta}.$$

The scattering amplitude $f(\theta',\varphi')$ is to be determined from the nature of the scattering center as it appears in transformed system.

To find the scattering cross section we must first calculate the radial current in the unprimed coordinates. This is done by taking

$$S_{\text{radial}}=S_x{}^2+S_y{}^2+S_z{}^2,$$

where the S_{x_i} are found by applying (A1) to (A4). Results, for real scattering amplitudes or for the s-wave scattering amplitude, which are the only ones we need consider, are best expressed in the form

$$S_{\text{radial}}=\hbar k'/m_d|f(\theta',\varphi')|^2(r/r'^3).$$

This expression together with (A2) yields a differential cross section of

$$d\sigma=(m_3/m_d)|f(\theta',\varphi')|^2(r^3/r'^3)d\Omega. \tag{A5}$$

To obtain the scattering cross section appropriate for transport (A5) must be multiplied by a factor[54]

$$1-\cos\theta_{\text{scat}},$$

where θ_{scat} is the angle between the incoming and scattered waves, and integrated over the surface of the unit sphere. For an incoming wave in the longitudinal direction $\cos\theta_{\text{scat}}=\cos\theta$. For the transverse direction $\cos\theta_{\text{scat}}=\sin\theta\cos\varphi$. For an incoming wave in the ith direction the scattering cross section is then given by

$$\sigma_i=\int_{4\pi}(1-\cos\theta_{\text{scat}})d\sigma. \tag{A6}$$

The relaxation time in the ith direction τ_i is found from the formula

$$\tau_i=1/nv_i\sigma_i, \tag{A7}$$

where v_i is the velocity of the incoming particle in the ith direction and σ_i is the corresponding scattering cross section. n is the number density of scatterers. Since the τ's that interest us will be functions of E only, the resistivity, for the case $T=0$ will be given by

$$\rho_i^{-1}=ne^2\tau_i(E_f)/m_i, \tag{A8}$$

where n now refers to the carrier density which we assume to equal the number density of scatterers, and e is the electronic charge. For the case of unstrained germanium the cubic symmetry yields a total resistivity[55] of

$$\rho^{-1}=\frac{ne^2}{3}\left(2\frac{\tau_1}{m_1}+\frac{\tau_3}{m_3}\right). \tag{A9}$$

---

[53] Cf., Ref. 52, p. 23.

[54] Cf., Ref. 2, p. 95.

[55] Cf., Ref. 2, p. 99.

The relaxation time components depend, in general, on the nature of the scattering potential and the approximation made in determining the scattering amplitude from the potential. In the Brooks-Herring and Gulyaev treatment of impurity scattering the screened Coulomb potential is used, i.e.,

$$V(\mathbf{r})=-(e^2/\epsilon r)e^{-r/R}, \tag{A10}$$

where R is the Fermi-Thomas screening length calculated by Dingle.[28] If we use the density-of-states mass appropriate to germanium and include the number of valleys t, we find that at $T=0$

$$R=7.8\times10^{-8}\epsilon^{1/2}N^{-1/6}t^{-1/3}\text{ cm},$$

where N is in units of $10^{18}/\text{cm}^3$. In the Conwell-Weisskopf case, the unscreened Coulomb potential is used.

Case 1: $ka\ll1$ Gulyaev Treatment of Ionized Impurity Scattering

In this case, we would like to make a partial-wave expansion and neglect all but the zeroth-order phase shift.[56] However, the partial-wave expansion is only appropriate where the scattering potential has spherical symmetry and the $V(\mathbf{r})$ given by (A10) does not have spherical symmetry in the primed system. This difficulty is avoided by taking a spherical potential as outlined in the text. S-wave scattering yields

$$|f(\theta',\varphi')|^2=\sin^2\delta_0/k'^2, \tag{A11}$$

where $\sin^2\delta_0$ may be determined from Gulyaev's formula (3.2). Applying (A5)–(A9) to the unstrained case yields

$$\rho_{4-\text{G}}=3.24(1+\cot^2\delta_0(4))N^{-1/3}\text{ m}\Omega\text{ cm}, \tag{A12}$$

where

$$\cot\delta_0(4)=2.16\times10^{-4}N^{2/3}\epsilon^2+4.70\times10^{-2}N^{1/3}\epsilon+4.80\times10^{-2}N^{1/6}\epsilon^{1/2}-5.12N^{-1/6}\epsilon^{-1/2}+2.55.$$

For the one-valley case the longitudinal resistivity is

$$\rho_{3-\text{G}}=27.4(1+\cot^2\delta_0(1))N^{-1/3}\text{ m}\Omega\text{ cm} \tag{A13}$$

and the transverse resistivity is

$$\rho_{1-\text{G}}=1.39(1+\cot^2\delta_0(1))N^{-1/3}\text{ m}\Omega\text{ cm},$$

where

$$\cot\delta_0(1)=2.18\times10^{-3}N^{2/3}\epsilon^2+7.45\times10^{-2}N^{1/3}\epsilon+1.21\times10^{-1}N^{1/6}\epsilon^{1/2}-2.07N^{-1/6}D^{-1/2}+0.638.$$

Case 2: $ka\gg1$ The Brooks-Herring Treatment of Ionized Impurity Scattering

Following the Brooks-Herring formulation, we use the Born approximation to calculate the scattering amplitude for the screened Coulomb potential. Applying Merzbacher's[57] formula (12.36) to the screened Coulomb potential in the primed coordinates yields

$$f(\theta')=-\frac{2m_d}{\hbar^2}\left(-\frac{e^2}{\epsilon}\right)\frac{1}{[2k'^2(1-\cos\theta_{\text{scat}})+R^{-2}]}, \tag{A14}$$

where R is the Fermi-Thomas screening length. Following (A5)–(A9) yields

$$\rho_{4-\text{BH}}=338.5\left[\frac{1}{J_3{}^4}+\frac{39.36}{J_1{}^4}\right]^{-1}N^{1/3}\epsilon^{-2}\text{ m}\Omega\text{ cm} \tag{A15}$$

for the unstrained case; the longitudinal and transverse resistivities for the one-valley case are given by

$$\rho_{3-\text{BH}}=179.1J_3{}^1N^{1/3}\epsilon^{-2}\text{ m}\Omega\text{ cm}$$

and

$$\rho_{1-\text{BH}}=9.10J_1{}^1N^{1/3}\epsilon^{-2}\text{ m}\Omega\text{ cm}, \tag{A16}$$

respectively, where

$$\begin{aligned}J_3{}^t&=\int_{4\pi}\frac{(1-\cos\theta)\sin\theta d\theta d\varphi(0.0813\sin^2\theta+1.60\cos^2\theta)^{-3/2}}{[(N/t)^{2/3}\{1-\cos\theta/(0.0508\sin^2\theta+\cos^2\theta)^{1/2}\}+8.558(t^{2/3}N^{1/3}/\epsilon)]^2},\\ J_1{}^t&=\int_{4\pi}\frac{(1-\sin\theta\cos\varphi)\sin\theta d\theta d\varphi(0.0813\sin^2\theta+1.60\cos^2\theta)^{-3/2}}{[(N/t)^{2/3}\{1-\sin\theta\cos\varphi/(\sin^2\theta+19.68\cos^2\theta)^{1/2}\}+8.558(t^{2/3}N^{1/3}/\epsilon)]^2}.\end{aligned} \tag{A17}$$

Case 3: Conwell-Weisskopf Treatment of Ionized Impurity Scattering

In this case the Rutherford scattering cross section is assumed, i.e.,

$$|f(\theta',\varphi')|^2=4\left(\frac{2e^2}{\epsilon E}\right)^2\csc^4\left(\frac{\theta_{\text{scat}}'}{2}\right),$$

where for an incoming particle in the longitudinal direction $\cos\theta_{\text{scat}}'=\cos\theta'$ and for a transverse direction $\cos\theta_{\text{scat}}'=\sin\theta'\cos\varphi'$. In addition, small-angle scattering is excluded from the integral (A6), i.e., the scattering of incoming particles whose impact parameter is larger than one half the interimpurity distance is neglected. The results are the same [(A15) and (A16)] as the Brooks-Herring treatment except for a change in the integrals $J_1{}^t$ and $J_3{}^t$. In the Conwell-Weisskopf

---

[56] Cf., Ref. 52, p. 106.

[57] E. Merzbacher, *Quantum Mechanics* (John Wiley & Sons Inc., New York, 1961), p. 227.

approximation

$$J_3{}^t=\int_{\theta_{\min}}^{\pi} d\theta \int_0^{\pi} d\varphi \times\frac{2(1-\cos\theta)\sin\theta(0.0813\sin^2\theta+1.60\cos^2\theta)^{-3/2}}{[(N/t)^{2/3}\{1-\cos\theta/(0.0508\sin^2\theta+\cos^2\theta)^{1/2}\}]^2}$$

and

$$J_1{}^t=\int_0^{\pi} d\theta \int_{\varphi_{\min}(\theta)}^{\pi} d\varphi \times\frac{2(1-\sin\theta\cos\varphi)\sin\theta(0.0813\sin^2\theta+1.60\cos^2\theta)^{-3/2}}{[(N/t)^{2/3}\{1-\sin\theta\cos\varphi/(\sin^2\theta+19.68\cos^2\theta)^{1/2}\}]^2},$$

where

$$\frac{\cos\theta_{\min}}{[0.0508\sin^2\theta_{\min}+\cos^2\theta_{\min}]}=\cos\left[2\arctan\left(8.67\frac{t^{2/3}}{N^{1/3}\epsilon}\right)\right]$$

and

$$\varphi_{\min}(\theta)=\text{arc}\cos\left\{\frac{(\sin^2\theta+19.68\cos^2\theta)^{1/2}}{\sin\theta}\times\cos\left[2\arctan\left(8.67\frac{t^{2/3}}{N^{1/3}\epsilon}\right)\right]\right\}.$$

APPENDIX B

The Mansfield model predicts a decreasing resistivity in the one-valley case (Table X) and an increasing resistivity is anticipated in the four-valley case (Table IX). This can be understood as follows:

The differential scattering cross section for a screened Coulomb potential is proportional to[58]

$$(1/(K^2+a^{-2}))^2, \tag{B1}$$

where K^2 is proportional to the energy of the carrier and a is the screening length. For an increase in temperature from 0°K the average carrier energy increases, thereby decreasing the scattering cross section and resistivity. The square of the inverse screening length, on the other hand, is given by[43]

$$a^{-2}=t\frac{16\pi^2e^2(2m_d)^{3/2}(kT)^{1/2}}{\epsilon h^3}f_{1/2}{}'(\eta^*) \tag{B2}$$

and decreases for an increase in temperature from 0°K and tends to increase the resistivity. (The number of valleys t is not found in the original expression.) The relative sizes of K^2 and a^{-2} in the four-valley case for the impurity concentrations under consideration are such that the temperature dependence of the inverse screening length dominates the affect and the temperature coefficient of resistivity is positive. In the one-valley case, however, the average carrier energy is $4^{2/3}$ times greater than for the corresponding doping in the four-valley case and the square of the inverse screening length is down by a factor of $4^{2/3}$. The K^2 term then becomes the important one and a negative temperature coefficient results.

APPENDIX C

The Fermi distribution function for an isolated system conserving energy and momentum may be written[59]

$$f(\epsilon)=\left(e^{\frac{\epsilon-\mathbf{u}\cdot\mathbf{p}-\epsilon_F}{kT}}+1\right)^{-1}, \tag{C1}$$

where ϵ and $\mathbf{p}$ are the carrier energy and momentum, respectively, and ϵ_F, the Fermi energy, and $\mathbf{u}$ are constants. In the case of small $\mathbf{u}$, i.e., $|\mu|\ll|v_F|$, Eq. (C1) may be written

$$f(\epsilon)=f_0(\epsilon)-\mathbf{u}\cdot\mathbf{p}(\partial f_0/\partial\epsilon), \tag{C2}$$

where $f_0(\epsilon)=\{\exp[(\epsilon-\epsilon_F)/kT]+1\}^{-1}$ is the usual Fermi distribution function. Using Eq. (C2) it is easy to show that the vector $\mathbf{u}$ corresponds to the drift velocity of the system in equilibrium.

Now consider the electron gas under the influence of a small external electric field $\mathbf{E}$ and a dissipative scattering mechanism described by a relaxation time τ. In the usual relaxation time approximation the distribution function for the system is

$$f(\epsilon)=f_0(\epsilon)-\tau e\mathbf{E}\cdot(\nabla_p\epsilon)(\partial f_0/\partial\epsilon) \tag{C3}$$

and for the case of one-valley germanium

$$\nabla_p\epsilon=\textstyle\sum_i(p_i/m_i)\hat{i}_i, \tag{C4}$$

where the Cartesian basis vectors $\hat{i}_i$ are chosen along the principal axes of the valley. This yields

$$f(\epsilon)=f_0(\epsilon)-\mathbf{O}\cdot\mathbf{p}(\partial f_0/\partial\epsilon), \tag{C5}$$

where the components of $\mathbf{O}$ are given by

$$\mathbf{O}_i=e\tau E_i/m_i. \tag{C6}$$

Comparing with Eq. (C2) we see that the distribution (C5) is an equilibrium distribution of the system, with drift velocity $\mathbf{O}$, and consequently will not be relaxed by interactions between the electrons. Therefore, electron-electron interactions cannot contribute to the resistivity in the one-valley case.

In the four-valley case the valley geometry changes Eq. (C4) and consequently, the simple form of (C5) is destroyed. The resulting distribution is not an equilibrium distribution if electron-electron interaction are allowed and the resistivity is affected.

It remains to be remarked that any anisotropy in τ will have the symmetry of the valley and is easily accounted for in Eq. (C6). Also, under typical experimental conditions $|\mathbf{u}|\approx 10$ cm/sec and $|v_F|>10^6$ cm/sec so that $|\mu|\ll|v_F|$ is indeed satisfied.

---

[58] Cf., Ref. 52, p. 170.

[59] This may be shown using the methods of D. ter Haar, *Elements of Statistical Mechanics* (Rinehart and Company, Inc., New York, 1954), Chap. 4.